OGLE-2012-BLG-0950Lb: THE POSSIBLE FIRST PLANET MASS MEASUREMENT FROM ONLY MICROLENS PARALLAX AND LENS FLUX

N. Koshimoto[1,m], A. Udalski[2,o], J.P. Beaulieu[3,p], T.Sumi[1,m], D.P. Bennett[4,5,m], I.A. Bond[6,m], N. Rattenbury[7,m], A. Fukui[8,m], V. Batista[3,p], J.B. Marquette[3,p], S.Brillant[9,p]

and

F. Abe[10], Y. Asakura[10], A. Bhattacharya[4,5], M. Freeman[7], Y. Hirao[1], Y. Itow[10], M.C.A. Li[7], C.H. Ling[6], K. Masuda[10], Y. Matsubara[10], T. Matsuo[1], Y. Muraki[10], K. Ohnishi[11], H. Oyokawa[10], To. Saito[12], A. Sharan[7], H. Shibai[1], D.J. Sullivan[13], D. Suzuki[4,5], P.J. Tristram[14], A. Yonehara[15]
(MOA Collaboration)

S. Kozłowski[2], P. Pietrukowicz[2], R. Poleski[2,16], J. Skowron[2], I. Soszyński[2], M. K. Szymański[2], K. Ulaczyk[2], Ł. Wyrzykowski[2]
(OGLE Collaboration)

ABSTRACT

We report the discovery of a microlensing planet OGLE-2012-BLG-0950Lb with the planet/host mass ratio of $q \simeq 2 \times 10^{-4}$. A long term distortion detected in both MOA and OGLE light curve can be explained by the microlens parallax due to the Earth's orbital motion around the Sun. Although the finite source effect is not detected, we obtain the lens flux by the high resolution Keck AO observation. Combining the microlens parallax and the lens flux reveal the nature

[1]Department of Earth and Space Science, Graduate School of Science, Osaka University, 1-1 Machikaneyama, Toyonaka, Osaka 560-0043, Japan

[2]Warsaw University Observatory, Al. Ujazdowskie 4, 00-478 Warszawa, Poland

[3]Sorbonne Universites, CNRS, UPMC Univ Paris 06, UMR 7095, Institut d'Astrophysique de Paris, F-75014, Paris, France

[4]Department of Physics, University of Notre Dame, Notre Dame, IN 46556, USA

[5]Laboratory for Exoplanets and Stellar Astrophysics, NASA/Goddard Space Flight Center, Greenbelt, MD 20771, USA

[6]Institute of Information and Mathematical Sciences, Massey University, Private Bag 102-904, North Shore Mail Centre, Auckland, New Zealand

[7]Department of Physics, University of Auckland, Private Bag 92019, Auckland, New Zealand

[8]Okayama Astrophysical Observatory, National Astronomical Observatory, 3037-5 Honjo, Kamogata, Asakuchi, Okayama 719-0232, Japan

[9]European Southern Observatory (ESO), Karl-Schwarzschildst. 2, D-85748 Garching, Germany

[10]Institute for Space-Earth Environmental Research, Nagoya University, Nagoya 464-8601, Japan

[11]Nagano National College of Technology, Nagano 381-8550, Japan

[12]Tokyo Metropolitan College of Industrial Technology, Tokyo 116-8523, Japan

[13]School of Chemical and Physical Sciences, Victoria University, Wellington, New Zealand

[14]Mt. John Observatory, P.O. Box 56, Lake Tekapo 8770, New Zealand

[15]Department of Physics, Faculty of Science, Kyoto Sangyo University, Kyoto 603-8555, Japan

[16]Department of Astronomy, The Ohio State University, 140 West 18th Avenue, Columbus, OH 43210, USA

[m]Microlensing Observations in Astrophysics (MOA) Collaboration

[o]Optical Gravitational Lensing Experiment (OGLE) Collaboration

[p]Probing Lensing Anomalies NETwork (PLANET) Collaboration

of the lens: a planet with mass of $M_{\rm p} = 35^{+17}_{-9} M_\oplus$ is orbiting around a M-dwarf with mass of $M_{\rm h} = 0.56^{+0.12}_{-0.16} M_\odot$ with a planet-host projected separation of $r_\perp = 2.7^{+0.6}_{-0.7}$ AU located at $D_{\rm L} = 3.0^{+0.8}_{-1.1}$ kpc from us. This is the first mass measurement from only microlens parallax and the lens flux without the finite source effect. The long term distortion can also be explained by the source orbital motion (xallarap) which is suspicious but not ruled out. These models can be distinguished by future high resolution imaging because of the much larger lens-source relative proper motion and brighter lens in the parallax model compared to the xallarap model. In the coming space observation-era with *Spitzer*, *K2*, *Euclid*, and *WFIRST*, we expect many such events for which we will not be able to measure any finite source effect. This work demonstrates an ability of mass measurements in such events.

Subject headings: gravitational lensing, planetary systems

1. Introduction

Gravitational microlensing is a technique by which planets can be detected without measurements of light from the host star (Mao & Paczynski 1991; Gould & Loeb 1992; Gaudi 2012). Microlensing can detect planets that are difficult to detect by other methods such as planetary systems in the Galactic Bulge (e.g., Batista et al. 2014), planets around late M-dwarfs or brown dwarfs (Bennett et al. 2008; Sumi et al. 2016), and even free floating planets not hosted by any stars (Sumi et al. 2011). Compared to other techniques, microlensing is sensitive to Earth mass planets (Bennett & Rhie 1996) orbiting just outside of the snow line where the core accretion theory (Ida & Lin 2004) predicts is the most active planet formation region. Microlensing observations so far have revealed a population of planets beyond the snow line (Gould et al. 2010; Sumi et al. 2010; Cassan et al. 2012; Shvartzvald et al. 2016; Suzuki et al. 2016). Suzuki et al. (2016) finds a steeper slope with $dN/d\log q \sim q^{-0.9}$ and a break (and possible peak) in the mass ratio function at $q \sim 1.0 \times 10^{-4}$. We are capable of studying the distance distribution of planets in our Galaxy via microlensing. Penny et al. (2016) suggests the possibility of a lack of planets in the Galactic bulge. The detection of extra solar planets by gravitational microlensing presents a number of challenges.

Firstly, gravitational microlensing is an extremely rare phenomenon with a probability of one per one million stars and a planetary deviation lasts for only hours or a few days. For these reasons, microlensing observations for exoplanets are conducted towards the Galactic bulge, the most crowded field in our Galaxy. However, the high degree of crowding causes serious blending problems owing to seeing effects imposed by the Earth's atmosphere, which

decrease the signal-to-noise ratio of events. Because of that, it is difficult to detect planets by ground-based survey observations. Whereas hundreds of planets are detected by the radial velocity (RV) method (Butler et al. 2006; Bonfils et al. 2013) and thousands of planetary candidates are detected by the *Kepler* telescope (Borucki et al. 2010) to date, the microlensing method has been used to detect about 50 exoplanets so far. In addition, the existence of daytime also makes the detection of planets difficult by ground-based observation. To cover 24 hours as fully as possible, several survey groups have been conducting high cadence survey observations using their telescopes with wide FOV cameras in different time zones. The Microlensing Observations in Astrophysics (MOA; Bond et al. 2001, Sumi et al. 2003) group uses the 2.2-deg^2 FOV MOA-cam3 (Sako et al. 2008) CCD camera mounted on the 1.8 m MOA-II telescope at the Mt. John University Observatory in New Zealand and alerts the community about 600 microlensing events per year. The Optical Gravitational Lensing Experiment group (OGLE; Udalski 2003) upgraded their camera to the 1.4-deg^2 FOV OGLE-IV camera in 2010 (Udalski et al. 2015a) and discovered more than 2000 microlensing events per year in the last few years with the camera mounted on the 1.3 m Warsaw telescope at the Las Campanas Observatory, Chile. The Wise observatory group in Israel also conducts microlensing observations (Gorbikov et al. 2010). In 2014, the Korean Microlensing Telescope Network (KMTNet; Kim et al. 2016) also started their survey observations. Now the equipment requirements for second-generation microlensing surveys (Gaudi et al. 2009; Gaudi 2012) are fulfilled and the number of planet detections is increasing over the next few years.

Measuring the mass and distance of a lens system is challenging. There are three observables in microlensing which can yield a mass-distance relation of the lens system: the angular Einstein radius $\theta_{\rm E}$, the microlens parallax $\pi_{\rm E}$, and the lens flux. One can calculate the mass and distance of the lens system if we can measure any two of these quantities. We can measure $\theta_{\rm E}$ in the following manner. Included in most models explaining planetary microlensing light curve data is the source star radius in units of $\theta_{\rm E}$: $\rho \equiv \theta_*/\theta_{\rm E}$. By estimating the angular radius of the source star, θ_*, by an analysis of the source star's color and magnitude, and using our modeled value of ρ, we arrive at an estimate of $\theta_{\rm E}$. Microlens parallax can be observed only in relatively rare events and lens flux measurements need follow-up observations with high resolution imaging by an 8-m class telescope. Therefore only half of planetary events published so far are detected with lens mass measurements and masses of the other half planetary systems are just given their probability distributions by a Bayesian analysis (e.g., Beaulieu et al. 2006; Bennett et al.2014; Koshimoto et al.2014; Skowron et al 2015). In the microlensing planetary events published so far, there are events with the mass measurements from the angular Einstein radius and microlens parallax (e.g., Bennett et al. 2008; Gaudi et al. 2008; Muraki et al. 2011), from the angular Einstein radius

and the lens flux (e.g., Bennett et al. 2006; Batista et al. 2015; Bennett et al. 2015), and from all three relations (e.g., Dong et al. 2009; Bennett et al. 2010; Beaulieu et al. 2016; Bennett et al. 2016), but events with mass measurement from only microlens parallax and the lens flux have not been published to date. This is simply because the angular Einstein radius is observed much commonly than microlens parallax as mentioned above. However, it has been possible to measure precise microlens parallax by observing simultaneously from space and ground thanks to the *Spitzer* microlensing campaign (Calchi Novati et al. 2015; Udalski et al. 2015b; Yee et al. 2015; Zhu et al. 2015). Also, *K2* campaign 9 (*K2*C9), started in April 2016, has surveyed the Galactic bulge for three months to date. By combining *K2*C9 data and ground-based survey data, it is expected to measure microlens parallax for more than 120 events (Henderson et al. 2015). These next generation space- and ground-based simultaneous observations for microlensing can measure microlens parallax almost regardless of the event timescale. Microlens parallax should become a more common observable rather than the angular Einstein radius in coming next generation, thus the mass measurement without the angular Einstein radius should be important (Yee 2015).

This paper reports an analysis of a microlensing planetary event OGLE-2012-BLG-0950, which is the first event where a mass measurement is possible from only the measurements of the microlens parallax and lens flux. The survey observations of this event are described in Section 2. Section 3 explains our data reduction procedure. Section 4 shows our modeling results. We show the constraint on the angular Einstein radius by the source angular radius derived from the color and light curve modeling in Section 5. We describe our Keck observations and the constraints on the excess flux in Section 6. In Section 7, we derive the lens properties by combining microlens parallax and the lens flux for the parallax model and conduct a Bayesian analysis for the xallarap model. Finally, Section 8 discusses and concludes the results of this work.

2. Observations

Microlensing event OGLE-2012-BLG-0950 was discovered and alerted by the OGLE Early Warning System (EWS) on 21 June 2012 (HJD$' \equiv$ HJD - 2450000 $\sim$ 6100) as a new event located at $(R.A., Dec.)_{J2000}$ = (18:08:04.62, -29:43:53.7) or $(l, b) = (1.765^\circ, -4.634^\circ)$. Another survey group, MOA, independently found the event and alerted that as MOA-2012-BLG-527 on 9 August 2012. The observations by OGLE were conducted on the I-band and V-band and the observations by MOA were conducted by the custom MOA-Red filter which is similar to the sum of the standard Cousins R- and I-band filters. MOA also observed the event in the I-band using the B&C telescope, a 61 cm telescope for follow-up

observation at the same site. The observed light curve is shown in Figure 1. The anomaly part of this event appeared as a small dip around HJD$' \sim 6149$ mainly in the MOA data. The MOA-II telescope observed the anomaly with the 47 minute cadence as the regular survey mode. Because the anomaly was very short, $\sim$1 day and started after the last OGLE observation, we could not to increase the cadence nor issue the anomaly alert in a timely manner. Nevertheless, the normal cadence is enough to reveal the perturbation caused by planet. The OGLE data with a cadence of once per night until the anomaly, are also very important for the characterization of this event. In particular, the OGLE data shows us that the dip had not started by HJD$' \simeq 6147.6$, had commenced by HJD$' \simeq 6148.6$ and had almost ended by HJD$' \simeq 6149.6$. This event does not cross any caustic curves and, unfortunately, MOA could not obtain data on HJD$' \sim 6148$, which corresponds to the start of the anomaly owing to bad weather. Because of these factors, we have no data on a steep gradient of magnification in this event, thus we cannot detect a significant finite source effect. In addition, we took AO images of the target in the year following the discovery, using the Keck telescope. We describe the details of the Keck observations and the analysis in Section 6.

3. Data reductions

Our data-sets for the modeling below consist of 1275 OGLE I-band data points, 81 OGLE V-band data points, 6324 MOA-Red data points and 382 B&C I-band data points.

The OGLE data were reduced by the OGLE Difference Image Analysis (DIA) photometry pipeline (Udalski 2003). The centroid of the catalogued star near the event, which is used for PSF photometry in the standard OGLE pipeline, is significantly different from that of actual event on the difference image. So, we rerun the PSF photometry with the real centroid for the event manually to obtain more accurate photometry.

The images taken by the MOA-II telescope and the B&C telescope were reduced by the MOA DIA pipeline (Bond et al. 2001). In the crowded stellar field images of the Galactic bulge, the precision of photometry is very sensitive to seeing. We found a systematic photometry bias correlated with the seeing value in the MOA-Red data. We reduced this systematic error by modeling it with a polynomial of seeing and airmass by using the baseline. In the resulting photometry, the χ^2 goodness-of-fit value for the time series of baseline is improved by $\Delta\chi^2 \sim 0.07$ per data point.

The relative error of data points given by the photometry code are robust for a given instrument. However it is known that the absolutely value of uncertainty are underestimated

in such stellar crowded fields for various reasons in general. Thus we empirically normalize the errors in each data-set to estimate the proper uncertainties of fitted model parameters. We used the formula presented in Yee et al. (2012) for normalization, $\sigma_i' = k\sqrt{\sigma_i^2 + e_{\rm min}^2}$ where σ_i is the original error of the ith data point in magnitudes, and the parameters for normalization are k and $e_{\rm min}$. k and $e_{\rm min}$ are adjusted so that the cumulative χ^2 distribution as a function of the number of data points sorted by each magnification of the preliminary best-fit model is a straight line of slope 1. By including $e_{\rm min}$, we can correct the error bars at high magnification, which can be affected by flat-fielding errors. But we found unusually large $e_{\rm min}$ values for the OGLE I and MOA-Red data (0.02 and 0.09 respectively) and the deviations from a straight line in cumulative χ^2 distribution mainly arose from baseline data points, i.e., not from high magnification data points as expected. Thus it is not reasonable to normalize errors with this values and we adopt $e_{\rm min} = 0$ for these two data-sets. This may indicate that there is some low-level systematics in the light curve. We apply $e_{\rm min} = 0,\ k = 1.364$ to OGLE I, $e_{\rm min} = 0,\ k = 1.576$ to OGLE V, $e_{\rm min} = 0,\ k = 0.907$ to MOA-Red and $e_{\rm min} = 0.0061, k = 1.021$ to B&C I. The normalization factors applied for the OGLE I and V data are consistent with those given by Skowron et al. (2016a). Note that the final best fit model parameters are consistent with the preliminary model parameters before the error normalization. Thus this procedure of the error normalization does not affect out main result. The parameters of these data sets are also shown in Table 1.

4. Modeling

Here we present and compare the results of light curve modeling with a standard binary lens and, in addition, adding either the effects of parallax or xallarap. We fit the light curves using a Markov Chain Monte Carlo (MCMC) approach (Verde et al. 2003), with magnification calculations from image centered ray-shooting method (Bennett & Rhie 1996; Bennett 2010).

4.1. Standard binary lens

In the case of a point lens, the magnification map on the source plane is circular symmetric around the lens. In the point source point lens (PSPL) case, we can characterize the microlensing light curve with the time of the closest approach of the lens and source, t_0, the minimum impact parameter u_0 at t_0, and the Einstein radius crossing time (or timescale) $t_{\rm E} = \theta_{\rm E}/\mu_{\rm rel}$, where u_0 is in units of $\theta_{\rm E}$ and $\mu_{\rm rel}$ is the lens-source relative proper motion. When the lens has a companion, its the gravity distort the magnification map and create

the closed curves called as caustics where the magnification is infinite. In this case, three parameters are added to the fitting parameters above; the mass ratio of two lenses q and their angular separation normalized by $\theta_{\rm E}$, s, which determine the shape and location of the caustics, and the source trajectory with respect to the binary lens axis, α, which determines the direction of a one-dimensional slice of the distorted magnification map. When a source star crosses a region with a steep gradient near the caustics in the magnification map, we can observe the finite source effect. Because source stars of most binary lens events cross such regions, we include the source size $\rho \equiv \theta_*/\theta_{\rm E}$ as a fitting parameter for a binary lens model. With the magnification variation against time, $A(t, \boldsymbol{x})$, which is defined in terms of the above parameters $\boldsymbol{x} = (t_0, u_0, t_{\rm E}, q, s, \alpha, \rho)$, we can linearly fit

$$F(t) = f_S A(t, \boldsymbol{x}) + f_b \tag{1}$$

to a data set and obtain the instrumental source flux f_S and the instrumental blending flux f_b for every telescope and pass-band.

We adopt a linear limb-darkening law with one parameter, u_λ. According to González Hernández & Bo (2009), we estimate the effective temperature, $T_{\rm eff} \sim 5500$ K from the source color which is discussed in Section 5 and assumed the solar metallicity. With $T_{\rm eff} = 5500$ K and assuming surface gravity $\log\ g = 4.0$ cm s^{-2} and microturbulence parameter $\xi = 1.0$ km s^{-1}, the limb-darkening coefficients selected from Claret (2000) are $u_I = 0.5470$ for OGLE I and B&C I, $u_V = 0.7086$ for OGLE V, and $u_{\rm MOA-Red} = 0.5895$ for MOA-Red which is the average of standard I and R filters. Therefore we used the u_I for OGLE I and B&C I, the u_V for OGLE V and the mean of the u_I and u_R, 0.5895 for MOA-Red, the filter which has the range of both the standard I and R filters. Although the best estimated value of $T_{\rm eff}$ and the limb-darkening coefficients depend on the source magnitude in each model, we keep using the fixed values. However, this does not affect our final result because the finite source effect is very weak in the light curve, as mentioned below. The limb-darkening coefficients we adopt are also shown in Table 1.

We show the parameters of the best-fit models of our standard binary lens modeling in Table 2. We find a degeneracy between the close model of $s < 1$ and the wide model of $s > 1$ with $\Delta\chi^2 \simeq 0.7$. There is a well-known degeneracy in high magnification microlensing events between lens systems with similar mass ratios, but separations s and $1/s$. In microlensing events suffering this degeneracy, the source star passes close to the central caustic which has, in each of the degenerate solutions, a similar shape. However, in this event, the close/wide degeneracy has a different nature, in terms of the caustic geometry. A single resonant caustic is seen in the wide model with $s = 1.007$ while the caustic curves are separated into central caustic and planetary caustics in the close model with $s = 0.890$. As seen in Figure 2, it is understood that the gradients of magnification on the source trajectories are similar in

both models although the caustic shapes are different. The mass ratios are $q \simeq 2 \times 10^{-4}$ in both models indicating the companion has a planetary mass. We find that the finite source effect is weak and the ρ value is consistent with $\rho = 0$ at the 1 σ level. Because a larger ρ value reduces the dip depth in the light curve and does not explain the data, we can place an upper limit on ρ.

4.2. Parallax

In long timescale microlensing events, such as this one, the effect of Earth's orbital motion around the Sun may be detectable (Gould 1992; Alcock et al. 1995). This effect is expressed by the microlens parallax vector $\boldsymbol{\pi_{\rm E}} = (\pi_{\rm E,N}, \pi_{\rm E,E}) = \pi_{\rm E}\ \boldsymbol{\mu_{\rm rel}}/\mu_{\rm rel}$ (Gould 2000). Here, $\pi_{\rm E,N}$ and $\pi_{\rm E,E}$ are the north and east components of $\boldsymbol{\pi_{\rm E}}$, respectively, whose direction is same as lens-source relative proper motion. The magnitude $\pi_{\rm E} \equiv 1{\rm AU}/\tilde{r}_{\rm E}$, is defined by 1 AU relative to the Einstein radius projected onto the observer plane $\tilde{r}_{\rm E} = R_{\rm E} D_S/(D_S - D_L)$.

We show our best-fit parallax models in Figure 1, 2 and Table 2. We found each close and wide solutions has an additional degeneracy between $u_0 > 0(+)$ and $u_0 < 0(-)$. These four degenerate solutions have $\Delta\chi^2 \lesssim 4$. The parameters of the degenerate models are consistent with each other to within 1σ error except for s, α and u_0. The χ^2 difference between the standard models and the parallax models is significantly large, $\Delta\chi^2 > 110$ for 2 dof difference.

It is known that low-level systematics in the baseline sometime mimic a high order signal. We therefore check whether the $\Delta\chi^2$ contributions come from where we theoretically expect. The top inset in Figure 3 shows the cumulative distribution for $\Delta\chi^2$ between the Standard close model and the Parallax close+ model as a function of time. Positive $\Delta\chi^2$ values indicate that the parallax model is favored over the standard model. We find $\Delta\chi^2 \sim 90$ comes from the data during the main peak of event in 2012 in both MOA and OGLE as expected, and $\Delta\chi^2 \sim 25$ comes from the data in 2013, the next year. The bottom right panel of Figure 1, which is a zoom of the 2013 data, shows slight differences among the models, i.e., the parallax models have the magnification of ~ 1.05 in the start of 2013 while the standard models have ~ 1.00. The bottom panel in Figure 3 shows binned residuals in bins 25 days wide. This shows the clear long term deviation from the standard model. The binned data in the first half of 2013 are mostly above the standard model in both MOA and OGLE whereas those in the other years are not, which can be well explained by the the parallax model. Because these long term distortion are consistent in both MOA and OGLE, we conclude that this long term signature are real and they are better explained by the parallax models compared to the standard models.

4.3. Xallarap

If the source star is in a binary system, the orbital motion of the source star can also measurably affect the trajectory of the source during a microlensing event. This effect, called xallarap, requires additional parameters which define orbital elements of the source system whereas we know the Earth's orbital elements for the parallax effect. This model require 7 additional fitting parameters, the direction toward the Earth relative to the source orbital plane, $R.A._{\xi}$ and $Dec._{\xi}$, which indicate the direction of the Earth to the source orbital plane, the orbital period P_{ξ}, the orbital eccentricity ϵ and the perihelion time $t_{\rm peri}$ in addition to $\boldsymbol{\xi_{\rm E}} = (\xi_{\rm E,N}, \xi_{\rm E,E})$ which is analogous to $\boldsymbol{\pi_{\rm E}}$ for microlens parallax. We omitted ϵ and $t_{\rm peri}$ as fitting parameters by assuming a circular orbit.

In xallarap fitting with no constraints, we found that the light curve prefers a solution with an unrealistically massive source companion with a mass of $M_C \sim 400\ M_{\odot}$. Thus we conducted the fitting with two constraints using information about the source system from our observations. The first constraint is on the hypothetical companion mass upper limit, enforced by the excess flux seen in our Keck observations and a mass function of the Galactic Bulge (e.g., Bensby et al. 2013), which is presented by Bennett et al. (2008). The second constraint is on the relationship between the projected separation of the hypothetical binary and the companion flux, enforced by the non-detection of any additional bump in the light curve by a microlensed source companion. Appendix A describes details of our xallarap modeling and compares the result with the parallax result. We show the best xallarap models in Table 2. As the conclusion, we find the best xallarap models, $\rm Xallarap^{\it K}_{bsf}$ have smaller χ^2 values compared to those of our best parallax models by $\Delta\chi^2 > 25$. The plausibility of our xallarap model seems to be suspicious because the preference of the xallarap model to the parallax model comes from only MOA data in 2013, the year following discovery. However we cannot exclude the xallarap scenario completely. We treat each case of parallax and xallarap in the discussion below. In $\rm Xallarap^{\it K}_{bsf}$ models, we got rough constraints on the source size ρ. Note that adding lens orbital motion does not improve our models.

5. The Angular Einstein Radius

We can place an upper limit on ρ for the parallax models and a lower limit as well for the xallarap models. It is possible to derive a constraint on $\theta_{\rm E} = \theta_*/\rho$ by obtaining the angular source radius θ_*. θ_* can be estimated from the source color, $(V-I)_S$, and the magnitude, I_S, empirically. We used the empirical relation by using a result of Boyajian et al. (2014) analysis,

$$\log\ [2\theta_*/(1{\rm mas})] = 0.5014 + 0.4197(V-I) - 0.2I. \qquad (2)$$

This relation comes from a private communication with them, which is restricted to FGK stars with 3900 K $< T_{\rm eff} <$ 7000 K and the accuracy of relation is better than 2% (Fukui et al. 2015). We measured the source color and brightnesses $(V-I, I)_S = (1.346, 19.29) \pm (0.001, 0.03)$ with the OGLE-IV instrumental magnitude from the light curve fitting. Note that because the source color and magnitudes are nearly identical for all models (see Table 2), we adopt values of Parallax close+ model in the following analysis. We correct their extinction following the standard procedure by Yoo et al. (2004) using the red clump giants (RCG) as a standard candle. Figure 4 shows a color-magnitude diagram (CMD) within the $2' \times 2'$ region around the source star with the OGLE-IV instrumental magnitude. The position of source and the measured RCG centroid $(V-I, I)_{RC} = (1.644, 15.27) \pm (0.011, 0.04)$ are shown as blue dot and red cross, respectively. Comparing the measured RCG centroid and the expected intrinsic position in this field $(V-I, I)_{RC,0} = (1.06, 14.38) \pm (0.07, 0.04)$ by Bensby et al. (2013) and Nataf et al. (2013), we obtain the intrinsic source color and magnitude as $(V-I, I)_{S,0} = (0.76, 18.40) \pm (0.07, 0.07)$ with the assumption that the source extinction are same as that the RCG. Note that the original reddening and extinction values in the standard magnitude in this field can be measured by the catalog of OGLE-III photometry map (Szymański et al. 2011) as $E(V-I) = 0.68 \pm 0.07$ and $A_I = 0.86 \pm 0.06$. We use these original values to obtain A_H in Section 6. Applying the intrinsic source color and magnitude to Equation (2), we obtain the angular source radius as $\theta_* = 0.69 \pm 0.05$ μas. From θ_*, ρ and $t_{\rm E}$, we can calculate the angular Einstein radius $\theta_{\rm E}$ and the lens-source relative proper motion μ_{rel},

$$\theta_{\rm E} = \theta_*/\rho > 0.22 \text{ mas}, \quad \mu_{rel} = \theta_{\rm E}/t_{\rm E} > 1.2 \text{ mas/yr}$$

for the Parallax close+ model, and

$$\theta_{\rm E} = 0.20^{+0.00}_{-0.09} \text{ mas}, \quad \mu_{rel} = 1.1^{+0.0}_{-0.5} \text{ mas/yr}$$

for the Xallarap$^K_{bsf}$ close+ model where the superscript of 0.0 means the best-fit value happens to be equal to the 84th percentile in the significant digit. Table 3 shows the derived parameters for all degenerate models using each models' values.

6. Excess Brightnesses from Keck AO Images

We have a mass-distance relation, i.e., the microlens parallax $\pi_{\rm E}$ for the parallax models and the angular Einstein radius $\theta_{\rm E}$ for the xallarap models. If we can measure the lens flux which give us an additional mass-distance relation, we could measure the mass and distance of the lens uniquely. We conducted high angular resolution observations using adaptive optics in order to measure the lens flux excluding as much flux from unrelated stars as possible.

6.1. Observations and the photometry

We observed OGLE-2012-BLG-0950 with the NIRC2 instrument on Keck II on July 18, 2013. We used the Wide camera with a pixel scale of 0.04 arcsec. We took 15 dithered H frames with an exposure time of 30 seconds. We performed dark and flatfield corrections in the standard way. Furthermore, OGLE-2012-BLG-0950 was observed as part of the VVV survey (Minniti et al. 2010) using the VISTA 4m telescope at ESO. We extracted 3 arcmin VVV JHK images centered on the target. We used the suite of tools developed as part of astr$O$matic (Bertin et al. 2002). We analysed the PSF of the images using PSFEx, then we measured the fluxes with SExtractor (Bertin & Arnouts 1996) using these PSF models. We cross identified 2MASS stars with VVV sources, and derived an absolute calibration of the VVV JHK images. We used the VVV images which we reprocessed as a reference to perform an astrometric calibration of one Keck frame. We then extracted the sources from this individual frame, and used them as a reference to realign all the Keck frames. We stacked the Keck frames with the SWARP tool (Bertin et al. 2002). We then performed aperture photometry on the Keck frame (for more details, see Batista et al. 2014). We cross identified common sources between Keck and VVV, and finally derived the calibration constant for KECK H band photometry.

Fig. 5 shows the field as observed by VVV and by Keck. First, we notice that the source in VVV is resolved in 2 objects with Keck. Using the astrometry on the amplified source, we are able to identify the source+lens of the microlensing as being the star that is marked on the frame. Its coordinates are $(R.A., Dec.)_{J2000}$ = (18:08:04.620, -29:43:53.43). It has a Keck H band magnitude of

$$H_{\rm target} = 16.89 \pm 0.02 \tag{3}$$

in the 2MASS magnitude system. The blend to the south is at coordinates $(R.A., Dec.)_{J2000}$ = (18:08:04.612, -29:43:53.88) and is slightly fainter at $H = 16.99 \pm 0.03$.

6.2. The excess flux

Considering a full width at half maximum of the target $\rm FWHM_{target} = 90$ mas in Keck image and the lens-source relative proper motion, $H_{\rm target}$ includes the lens flux plus the source flux. Here we derive the excess brightness by subtracting the source system brightness, which can be used as the lens flux or its upper limit. Hereafter we represent our derived values for only Parallax close+ model as the parallax model and for only Xallarap$^{K}_{bsf}$ close+ model as the xallarap model unless otherwise stated.

Unfortunately, we don't have a light curve in the H-band, so we derived the source

H magnitude as $H_{S,0} = 17.55 \pm 0.12$ by converting the magnitude from $(V-I, I)_{S,0}$ with the color-color relation by Bessell & Brett (1988). Next we applied the $E(V-I)$ and A_I values derived in Section 5 and estimated the extinction in H-band as $A_H = 0.25 \pm 0.02$ (Cardelli et al. 1989). The magnification at the time of Keck observation of HJD$' = 6491.88$ is $A = 1.005$ for the parallax model or $A = 1.020$ for the xallarap model. Thus the source apparent H magnitude at the time is $H_{S,\mathrm{KECK}} = 17.78 \pm 0.12$ for the parallax model or $H_{S,\mathrm{KECK}} = 17.73^{+0.16}_{-0.08}$ for the xallarap model. These values are converted to the 2MASS magnitude system from the Bessel & Brett system using Equations (A1) - (A4) in Carpenter (2001). Subtracting this from H_{target} of Equation (3), we derive the excess brightness of

$$H_{\mathrm{excess}} = 17.52 \pm 0.10 \tag{4}$$

for the parallax model. For the xallarap model, because H_{target} involves the flux of the source companion, we subtract it as well and obtain

$$H_{\mathrm{excess}} > 17.63. \tag{5}$$

As discussed in Appendix A and shown in Table 4, the uncertainty of the source companion flux is large as H_C=16.5 - 20.7 and we obtain only the brighter limit of the excess flux for the xallarap model.

7. Lens Properties

In this section, we constrain the lens properties for each of the parallax cases and the xallarap case. All results are summarized in Table 3.

7.1. The parallax solution - mass measurement

For the Parallax model, we have two mass-distance relations. One is the lens absolute magnitude,

$$M_{H,L} = H_L - A_{H,L} - 5\log\frac{D_L}{10\mathrm{pc}} \quad (H_L = H_{\mathrm{excess}} - 2.5\log(1-f)) \tag{6}$$

where f is the fraction of contamination flux to excess flux and $A_{H,L}$ is an extinction for the lens located at D_L and we adopted $A_{H,L} = A_H D_L / D_S$ following to Fukui et al. (2015). This is converted to a relationship between the host mass M_{h} and the distance D_L by using isochrone models from the PARSEC isochrones, version 1.2S (Bressan et al. 2012; Chen et al. 2014;

Tang et al. 2014; Chen et al. 2015). The other mass-distance relation is from the microlens parallax $\pi_{\rm E}$:

$$M_{\rm h} = \frac{1}{1+q}\frac{\pi_{\rm rel}}{\kappa \pi_{\rm E}^2} \tag{7}$$

where $\kappa = 8.144$ mas $M_\odot^{-1}$ and $\pi_{\rm rel} = {\rm AU}\ (1/D_L - 1/D_S)$.

The left panel in Figure 6 shows these two relations for the Parallax close+ model. Black lines are the mass-distance relation come from $\pi_{\rm E}$. The red, blue and green lines indicate the relation from $M_{H,L}$ for the case of f=0, 0.5 and 0.9, respectively. Dashed lines indicate 1 σ errors and they include the uncertainty of the distance to the source of $D_S = 8.0 \pm 1.6$ kpc, the lens age of < 13 Gyr and the lens metallicity of [Fe/H] $= -0.05 \pm 0.20$ in addition to the uncertainty of our measurements. We adopt the metallicity distribution of nearby M- or late K-dwarf stars (Gaidos et al. 2014, e.g.) for the metallicity. Note that the dependency on age is much weaker than that on metallicity in the region of the parallax solution. The region overlapping these two relations corresponds to the allowed solution. For $f = 0$, the host mass is $M_{\rm h} = 0.57^{+0.06}_{-0.10} M_\odot$ and the distance is $D_L = 2.6^{+0.5}_{-0.7}$ kpc, and the planet mass is $M_{\rm p} = 35^{+10}_{-6} M_\oplus$, its projected separation is $r_\perp = 2.6^{+0.3}_{-0.5}$ AU and the three-dimensional star-planet separation is statistically estimated as $a = 3.1^{+1.5}_{-0.7}$ AU with a circular orbit assumption (Gould & Loeb 1992). From this solution, we can calculate the angular Einstein radius and the relative lens-source proper motion as $\theta_{\rm E} = 1.09^{+0.16}_{-0.10}$ mas and $\mu_{\rm rel} = 5.8^{+0.8}_{-0.6}$ mas/yr, respectively. The solution of $M_{\rm h} = 0.50^{+0.05}_{-0.09} M_\odot$, $D_L = 2.9^{+0.6}_{-0.8}$ kpc for $f = 0.5$ is consistent with that for $f = 0$ within 1σ and the probabilities of $f \leq 0$ and $f \leq 0.5$ are 59.4% and 89.1% respectively. In addition, the solution for $f = 0.9$ is $M_{\rm h} = 0.33^{+0.05}_{-0.08} M_\odot$, $D_L = 3.6^{+0.6}_{-0.8}$ kpc and the probability of $f \leq 0.9$ is 95.4 %. Our estimate for these contamination probabilities is discussed in Appendix B. In any case, the host star is an M or K dwarf and the planet is a Neptune mass or sub-Saturn mass planet. All solutions of the other degenerate parallax models are similar to these results as shown in Table 3. We present the mean value of the 8 parallax solutions with $f = 0$ and $f = 0.5$ without any weight as "Mean" in Table 3. Here the contributions of solutions with $f > 0.5$ are negligible.

7.2. The xallarap solution - mass estimate

As described above and in Appendix A, we have one mass-distance relationship from the angular Einstein radius for the Xallarap$^K_{bsf}$ model;

$$M_{\rm h} = \frac{1}{1+q}\frac{\theta_{\rm E}^2}{\kappa \pi_{\rm rel}} \tag{8}$$

We also have a lower limit of H_L, $H_L > H_{L,\rm low} = 17.63$. We can place a lower limit of $M_{H,L}$ of $M_{H,L,\rm low} = H_{L,\rm low} - A_{H,L} - 5\log(D_L/10{\rm pc})$ by using Equation (6) with $H_{L,\rm low}$. The right panel in Figure 6 shows the mass-distance relation obtained from Equation 8 and $M_{H,L,\rm low}$. From their overlapped region, we obtain constraints on the host mass and the distance as $M_{\rm h} < 1.17 M_\odot$ and $D_L < 9.4$kpc, respectively. These constraints are very weak.

We cannot place stronger constraints on the lens parameters above solely from our observations. Thus we obtained a probability distribution of the lens parameters by conducting a Bayesian analysis assuming the Galactic model of Han & Gould (2003) (Alcock et al. 1995; Beaulieu et al. 2006; Gould et al. 2006; Bennett et al. 2008) as shown in Figure 7. We calculated the posterior probability by multiplying the likelihood from our measuring of $t_{\rm E}$, $\theta_{\rm E}$ and $H_{L,\rm low}$ by the prior probability from the Galactic model for each degenerate model and combine the posterior probabilities for close+, close−, wide+ and wide− models by weighting by $e^{-\Delta\chi^2/2}$. Our Bayesian analysis prefers a lens system which consists of a planet with mass of $M_p = 13^{+18}_{-7} M_\oplus$ orbiting around the host with mass of $M_{\rm h} = 0.19^{+0.26}_{-0.10} M_\odot$ with a semi-major axis of $a = 1.3^{+0.8}_{-0.4}$ AU located at $D_L = 6.7^{+1.1}_{-1.0}$ kpc. We also conduct another Bayesian analysis with the mass function by Sumi et al. (2011) including a planetary mass range because the right panel in Figure 6 implies a planetary mass host if the lens is nearby. But the results are identical. This is because the lens is expected to be in the Bulge in order to explain the very small value of $\mu_{\rm rel}$ of the Xallarap$^K_{bsf}$ models.

8. Discussion and Conclusion

We analyzed the microlensing event OGLE-2012-BLG-0950. A negative perturbation in the microlensing light curve consistent with a low-mass planet was detected (Abe et al. 2013). All the models we analyzed have a planetary mass ratio, $q \simeq 2 \times 10^{-4}$. We could not detect a significant finite source effect because the source did not cross any caustic. We have two competing solutions of lens physical properties. The parallax solutions indicate a Neptune or sub-Saturn mass planet around an M- or K-dwarf host. The xallarap solutions indicate a super-Earth or Neptune mass planet around an M-dwarf host. We measured the lens mass by combining microlens parallax and the lens flux obtained by Keck AO observations in the parallax scenario. This is the first case in which the lens mass was measured using only microlens parallax and the lens flux. On the other hand, in the xallarap scenario, we obtained the angular Einstein radius instead of microlens parallax thanks to our constraints on the source orbit. Obtainment of the angular Einstein radius is also the first case without a significant finite source effect or parallax effect. However, we could not place the fainter limit of the lens flux because we couldn't place the upper limit of the source companion

flux in the excess flux. Thus we performed a Bayesian analysis to derive the probability distributions of the lens physical properties for the xallarap models.

We cannot exclude the xallarap scenario completely although its plausibility is dubious (see Appendix A.3). The lens-source relative proper motions $\mu_{\rm rel}$ are measured for the parallax and xallarap models. The values of the parallax models are 4-6 times faster than those of the xallarap models. In addition, the implied lens brightnesses assuming the parallax models are $H_L = 17.5$ mag for $f = 0$ which are bright enough to be observed. Therefore we can distinguish between the parallax and the xallarap explanations by conducting a high resolution follow-up observation again in ~ 10 years, when one expect to be able to separate the lens from the source in the parallax scenario and not in the xallarap scenario. In addition to the parallax/xallarap degeneracy, this event suffers a close/wide and $u_0 > 0/u_0 < 0$ degeneracies. But these degeneracies do not matter because the resultant lens physical properties are all consistent within 1σ uncertainty.

If the parallax scenario is true, the planet orbits outside of the snow line of the host star and has a mass between that of Neptune and Saturn, $M_{\rm p} = 35^{+17}_{-9} M_\oplus$. Planets with this mass range (intermediate mass, hereafter) are predicted to be rare inside the snow line, but to be common like Neptune- or Saturn- mass planets outside the snow line according to the core accretion theory (Ida & Lin 2004; Ida et al. 2013). A paucity of intermediate mass planets orbiting close to their metal-poor host stars is confirmed (Beaugé & Nesvorný 2013). The "sub-Jovian desert" is suggested in this mass range at even closer orbits (period $\lesssim$ 2.5 days) (Szabó & Kiss 2011; Beaugé & Nesvorný 2013; Matsakos & Konigl 2016). On the other hand, the predicted relative abundance outside the snow line has not been confirmed yet. Figure 8 shows the distribution of the exoplanets[1] discovered so far. The solution of our parallax model is indicated as the purple filled circle located just around the valley of the bimodal mass distribution histogram on the left side of the figure. Note that this distribution is not corrected for detection efficiency. Only a few intermediate mass planets orbiting outside the snow line have been discovered by the RV and microlensing methods. The parallax model of this work could be the second such intermediate mass exoplanet with mass measurement, following OGLE-2012-BLG-0026Lb (Han et al. 2013; Beaulieu et al. 2016). The mass of other intermediate mass planets are estimated by Bayesian analysis (Miyake et al. 2011; Poleski et al. 2014; Skowron et al. 2016b). However the Bayesian estimates depend on the choice of prior (Bennett et al. 2014; Skowron et al. 2015).

In a future space-based microlensing survey by *WFIRST* (Spergel et al. 2015) and *Euclid* (Penny et al. 2013), or in the survey of Campaign 9 of the *K2* Mission (Henderson et al. 2015)

[1]http://exoplanet.eu

conducted from April 2016 to July 2016, it is very important to determine the lens mass for each event by combining microlens parallax and lens flux as pointed out by Yee (2015) for the following reasons. First, space- and ground-based simultaneous observations are expected to obtain microlens parallax for almost all events regardless of number of the lens bodies, in contrast to the finite source effect which can be obtained only by observing the peak of high-mag event or caustic crossing. Second, for low-mass and nearby lenses, the mass-distance relations derived from flux and from $\theta_{\rm E}$ are partially degenerate (see Figure 2 in Yee 2015 or Figure 7 in Fukui et al. 2015) although we can obtain $\theta_{\rm E}$ by the measurement of astrometric microlensing effects with the precision of *WFIRST* (Gould & Yee 2014). Third, the cases without detection of $\theta_{\rm E}$ like this event are expected to increase even for planetary events because a higher precision and higher cadence survey can detect more subtle planetary signals including cases without crossing caustics. Finally, it is possible to measure the lens fluxes even after the events by follow-up observations with high angular resolution, and ultimately, *WFIRST* and *Euclid* can routinely measure the lens fluxes as part of the survey observations. Our analysis for the parallax model is the first demonstration of the mass measurement from only microlens parallax and the lens flux, and thus it has particular significance for the developing era of space-based microlensing.

We acknowledge the following support: Work by N.K. is supported by JSPS KAKENHI Grant Number 15J01676. The MOA project is supported by the grant JSPS25103508 and 23340064. N.J.R is a Royal Society of New Zealand Rutherford Discovery Fellow. OGLE Team thanks Profs. M. Kubiak and G. Pietrzyński, former members of the OGLE team, for their contribution to the collection of the OGLE photometric data over the past years. The OGLE project has received funding from the National Science Centre, Poland, grant MAESTRO 2014/14/A/ST9/00121 to AU. V.B. was supported by the CNES and the DIM ACAV, Région Île-de-France. V.B., J.P.B., and J.B.M. acknowledge the support of PERSU Sorbonne Université, the Programme National de Planétologie and the labex ESEP.

A. Xallarap analysis

Here we describe our constraints for xallarap fitting, the results and comparison with the parallax model, and discuss the constraints.

A.1. Constraint by the companion mass upper limit

Kepler's 3rd law gives us a relation of the source orbit;

$$\xi_{\rm E} = \frac{\rm AU}{D_S\theta_*/\rho}\left(\frac{M_C}{M_\odot}\right)\left(\frac{M_\odot}{M_S+M_C}\frac{P_\xi}{1{\rm yr}}\right)^{2/3} \tag{A1}$$

where M_S and M_C are the masses of the source and its companion, respectively. We can place an upper limit of the companion mass $M_C < M_{C,\rm max}$ from Equation (4) of the excess flux with an assumption that the companion is not a stellar remnant. Then we can also place an upper limit of $\xi_{\rm E}$ as $\xi_{\rm E} < \xi_{\rm E,max}$ where $\xi_{\rm E,max}$ is defined as $\xi_{\rm E}$ of Equation (A1) with $M_C = M_{C,\rm max}$ (Bennett et al. 2008; Sumi et al. 2010). We applied the additional χ^2 presented by Bennett et al. (2008) to each link of MCMC fitting;

$$\chi^2_{\rm orb} = \Theta(\xi_{\rm E} - \xi_{\rm E,max})\left(\frac{\xi_{\rm E}-\xi_{\rm E,max}}{\sigma_{\xi_{\rm E,max}}}\right)^2 \tag{A2}$$

where Θ is the Heaviside step function and we applied 7% to $\sigma_{\xi_{\rm E,max}}$, the uncertainty of $\xi_{\rm E,max}$, with the consideration of uncertainty on θ_* as given in Section 5. We derive $D_S = 8.0 \pm 1.6$ kpc by a Bayesian analysis with the Galactic model (Han & Gould 2003) constrained by the observed $t_{\rm E}$ value, $M_S = 1.02 \pm 0.12 M_\odot$ and $M_{C,\rm max} = 1.10 \pm 0.19 M_\odot$ from the color and brightness of the source and blending. To calculate $\xi_{\rm E,max}$, we use the lower or upper limit value for each parameter so that it makes $\xi_{\rm E,max}$ larger for a conservative constraint, namely, we use $D_S = 6.4$ kpc, $M_S = 0.9 M_\odot$, $M_{C,\rm max} = 1.2 M_\odot$ for the calculation of $\xi_{\rm E,max}$ where $M_{C,\rm max} = 1.2 M_\odot$ comes from the Galactic mass function (Bensby et al. 2013). For ρ and P_ξ, we used each link's values to calculate the $\xi_{\rm E,max}$.

The "Xallarap^K" models in Table 2 are our results of xallarap fitting with a circular orbit and the $\xi_{\rm E,max}$ constraint above. We find smaller χ^2 values than that from the parallax models by $\Delta\chi^2 \gtrsim 27$. Note that including eccentricity intends to fit systematics in the baseline and does not improve a model significantly, so we don't consider eccentric orbits according to Occam's razor. Xallarap^K models place a lower limit on ρ whereas the other models above do not. This is because the $\xi_{\rm E,max}$ constraint is equivalent to placing a lower limit of ρ as

$$\xi_{\rm E} < \xi_{\rm E,max} \Leftrightarrow \rho > \rho_{\rm min} \equiv \frac{\theta_* D_S \xi_{\rm E}}{M_{C,\rm max}(M_{C,\rm max}+M_S)^{-2/3}P_\xi^{2/3}}. \tag{A3}$$

Combining it with the upper limit from the finite source effect, we can constrain the ρ value with $\sim 30\%$ uncertainty. This is the first case of ρ being constrained with neither a significant finite source effect nor a parallax effect.

We can calculate a $\theta_{\rm E}$ value from ρ and θ_*. In principle, we can determine a mass and distance of the lens star by combining the $\theta_{\rm E}$ and H_L, the lens flux in H-band extracted from Keck AO observations (Batista et al. 2014; Fukui et al. 2015, e.g.). However we encounter a problem with this. As shown in Table 4, the uncertainty of the mass of the companion to the source star in the Xallarap^K models is very large and the upper limit of $\sim 1.8 M_\odot$ is larger than $M_{C,\rm max} = 1.2 M_\odot$, the maximum mass of the companion we use in the $\xi_{\rm E,max}$ constraint. In other words, the lower limit of H_C, the apparent H magnitude of the companion, is brighter than the brightness limit as $H_C \simeq 16.2$ mag $< H_{\rm excess} \simeq 17.5$ mag where $H_{\rm excess}$ value comes from Equation (4). It means we cannot place a fainter limit on H_L, the lens brightness in the H-band. These excesses are attributed to the uncertainties of the parameters that determine $\xi_{\rm E,max}$, i.e., the uncertainties of D_S, M_S and θ_*. Especially, it is more sensitive to the uncertainties of θ_* and D_S rather than M_S due to the relation between M_C and the other parameters, $\xi_{\rm E} \propto (D_S \theta_*)^{-1} M_C (M_S + M_C)^{-2/3}$. We calculate a $\xi_{\rm E,max}$ value with the most conservative combination of D_S and M_S in their 1 σ uncertainties, $D_S = 6.4$ kpc and $M_S = 0.9 M_\odot$, so that they make the $\xi_{\rm E,max}$ largest in the 1 σ range. Then we judge a set of (ρ, P_ξ, $\xi_{\rm E}$) by the conservatively large $\xi_{\rm E,max}$ value and accept them up to 7% larger $\xi_{\rm E}$ than $\xi_{\rm E,max}$ considering the uncertainty on θ_*. Thus the M_C value range derived from the accepted parameters with $D_S = 8.0 \pm 1.6$ kpc and $M_S = 1.02 \pm 0.12 M_\odot$ can exceed its limit, $M_{C,\rm max} = 1.2 M_\odot$. Therefore, we cannot limit the possible taken region of the companion mass M_C within the maximum value of $M_{C,\rm max}$ by the $\xi_{\rm E,max}$ constraint as long as we conduct the fitting with the conservatively large $\xi_{\rm E,max}$ values. To avoid this problem, we need to include D_S, M_S, θ_* and isochrone models of the source system as additional fitting parameters in MCMC, which are generated according to their prior probability distributions. In each link, calculate a H_C value by an isochrone model with a M_C value calculated from Equation (A1) and reject the link if the H_C is brighter than a brightness limit from $H_{\rm excess}$. Then the accepted links should make feasible probability distributions for all parameters above and maybe we could place a fainter limit of H_L. However, such a calculation is too complicated to conduct and we know only a small number of stellar ages in the Galactic Bulge (e.g., Bensby et al. 2013) on which an isochrone model depends. Thus we don't consider such a complicated calculation. We instead consider an additional constraint by another observed fact with an aim to reduce the upper limit of M_C and to search for a more satisfactory xallarap model.

A.2. Constraint by undetected binary source signal

We can constrain the period of a binary star source system because we can detect an additional bump caused by a microlensed companion star in the light curve if it is close

enough to the source star to be magnified (Batista et al. 2014). Although it might need a simulation to verify if we can detect the binary source signal with sufficient signal-to-noise when we add a hypothetical companion, here we simply assume we can detect the signal at least with an amplitude larger than the parallax/xallarap signal we detected in the light curve. As we can find in the bottom inset in Figure 3, the OGLE I data in the light curve is sensitive enough to a deviation with an amplitude of $\Delta A \simeq 0.1$ and a duration of hundreds of days. That means we can detect a binary source signal when a companion to the source is magnified with an amplitude of $\gtrsim 0.1 f_S$ and a duration of hundreds of days. We cannot find such a small signal if it appears over a very long duration. We assume that we can detect the signal caused by a magnified companion to the source star when the time variation of the companion flux is larger than $0.1 f_S$ within 10 $t_{\rm E} \simeq 670$ days, that is, it requires

$$A(u_{C,0}) f_C - A\left(\sqrt{5^2 + u_{C,0}^2}\right) f_C \leq 0.1 f_S \tag{A4}$$

to be "undetected", and because $A\left(\sqrt{5^2 + u_{C,0}^2}\right) < A(5)$, we can express the condition more conservatively,

$$\begin{aligned} A(u_{C,0}) f_C - A(5) f_C &\leq 0.1 f_S \\ \Leftrightarrow u_{C,0} \geq u &\left(1.00275 + 0.1 \frac{f_S}{f_C}\right) \equiv u_{C,0,\rm low} \end{aligned} \tag{A5}$$

where $u_{C,0}$ and f_C are the impact parameter and the flux in I-band of the companion star, respectively. $A(u_C)$ is the magnification when the companion is located at u_C and we use the magnification of single lens $A(u) = (u^2+2)/u\sqrt{u^2+4}$ as $A(u_C)$. The $u_{C,0,\rm low}$ is a lower limit of the impact parameter of the companion to be undetected and it gives us a lower limit of the separation between the source and the companion as $s_{SC} > s_{SC,\rm low}$. When the time when the companion is located at $u_C = u_{C,0}$ is defined as $t_{C,0}$, it is possible to give the most conservative lower limit as $s_{SC} > s_{SC,\rm low} \equiv |u_{C,0,\rm low} - |u_0||$ when $t_{C,0} = t_0$ and the closest companion crosses the same side as the source relative to the lens. Thus we derive the lower limit of the semi-major axis of the source system as $a_{SC,\rm low} \equiv D_S \theta_{\rm E} s_{SC,\rm low}$. Applying Kepler's 3rd law to that, we can also place the lower limit of the period P_ξ as

$$P_\xi > P_{\xi,\rm low} \equiv 365.25 \text{ days} \left(\frac{M_S + M_C}{M_\odot}\right)^{-1/2} \left(\frac{a_{SC,\rm low}}{\rm AU}\right)^{3/2}. \tag{A6}$$

For example, when $M_C = M_S = 1 M_\odot \Leftrightarrow f_C = f_S$, $u_{C,0,\rm low} \simeq 1.7$ and assuming D_S =8kpc and $\theta_{\rm E} = 0.15$mas, the limits take $a_{SC,\rm low} \simeq 1.9$AU and $P_{\xi,\rm low} \simeq 705$ days. The best-fit period values in the Xallarap^K models are $P_\xi \sim 530$ days $< P_{\xi,\rm low}$. Thus in this example case, the best-fit Xallarap^K models are inconsistent assuming a binary source. If a candidate MCMC link corresponds to a brighter, heavier companion, $u_{C,0,\rm low}$ takes larger values, i.e.,

$P_{\xi,\rm low}$ takes larger values and the constraint becomes more effective. This means that the constraint works in the direction of making the companion mass M_C smaller.

In practice, we applied the additional χ^2 of

$$\chi^2_{\rm peri} = \Theta(P_{\xi,\rm low} - P_\xi) \left(\frac{P_{\xi,\rm low} - P_\xi}{\sigma_{P_{\xi,\rm low}}} \right)^2 \tag{A7}$$

to each link in the MCMC model fitting algorithm as well as $\chi^2_{\rm orb}$ because $P_{\xi,\rm low}$ has an uncertainty $\sigma_{P_{\xi,\rm low}}$, as well as $\sigma_{\xi_{\rm E,max}}$ for $\xi_{\rm E,max}$. To calculate $P_{\xi,\rm low}$, we adopted $D_S = 6.4$kpc, $M_S = 1.1 M_\odot$ and an isochrone model with age = 3 Gyr, [Fe/H] = 0.34 using the PARSEC isochrones version 1.2S (Bressan et al. 2012; Chen et al. 2014, 2015; Tang et al. 2014) for the calculation of $f_S/f_C = 10^{-0.4(M_{I,S} - M_{I,C})}$ in Equation (A5) where $M_{I,S}$ and $M_{I,C}$ are absolute I magnitudes of the source and the companion. These are selected within 1 σ errors of these values so that they make $P_{\xi,\rm low}$ smaller in consideration of getting the constraint more conservative. The age and metallicity come from those distribution of the Bulge stars by Bensby et al. (2013) and we selected the pair that makes $(dM_*/dM_I)_{M_*=1.1M_\odot}$ smallest in a $\sim 1\sigma$ region of the distribution because $P_{\xi,\rm low}$ takes the smallest values using this in the range of $\chi^2_{\rm peri} > 0$. We know information about the source brightness in two bands, V-band and I-band. Thus, in principle, with a given D_S, the consistency between two M_S values derived from $M_{V,S}$ and $M_{I,S}$ can generate a proper isochrone model and M_S. However, because it is too complicated to include the correlation among D_S, M_S and isochrone models in our fittings, we selected those parameters' values independently. Note that the uncertainty of the source brightness and the wide range distribution of the age and metalicity of bulge stars (e.g., Bensby et al. 2013; Gonzalez et al. 2015) are basically too large for us to determine M_S and the isochrone model only from the information of I-band and V-band values for a given D_S. Therefore we can select these parameters almost independently. In the isochrone model we adopted, stars with $M_* \gtrsim 1.45 M_\odot$ evolved off the main sequence. We calculate the $M_{I,C}$ value of the link with $M_C > 1.45 M_\odot$ by extrapolating the slope of $(dM_*/dM_I)_{M_*=1.44M_\odot}$ because we adopted the isochrone model in terms of making $(dM_*/dM_I)_{M_*=1.1M_\odot}$ smallest for a more conservative constraint, not for the consistency of the age and metallicity of the source system. Actually, the uncertainty of $P_{\xi,\rm low}$ is relatively large and we apply $\sigma_{P_{\xi,\rm low}} = 0.25 P_{\xi,\rm low}$, applying $\sim 7\%$ uncertainty in θ_*. Therefore the additional χ^2 takes $\chi^2_{\rm peri} \leq (P_{\xi,\rm low}/\sigma_{P_{\xi,\rm low}})^2 = 16$. Considering cases in which we cannot detect the binary source signal when it is too short and the S/N is not enough to be detected or the brightening occurs during a Bulge-off season even with the signal satisfying Equation (A5), we adopted $\chi^2_{\rm peri} = 0$ to the link with

$$t_{C,\rm FWHM} \equiv 2 t_{\rm E} \sqrt{u^2 \left(1 + \frac{A(u_{C,0,\rm low}) - 1}{2} \right) - u^2_{C,0,\rm low}} < 140 \text{days} \tag{A8}$$

where $t_{C,\mathrm{FWHM}}$ is the full width at half maximum of the microlensed time for the companion. This condition is equivalent to $u_{C,0,\mathrm{low}} \lesssim 1.2$ assigned with $t_{\mathrm{E}} \simeq 67$days.

We show the results of our xallarap fitting with the additional constraint as "Xallarap$^K_{bsf}$" in Table 2. The indicator, "bsf" means "binary source flux". Table 4 shows 1 σ ranges of M_C, H_C and $P_{\xi,\mathrm{low}}$ values calculated on Xallarap^K models and Xallarap$^K_{bsf}$ models. Also, Figure 9 shows the MCMC chain distributions of the parameters used for constraint for the Xallarap^K close+ model and the Xallarap$^K_{bsf}$ close+ model. Note that the M_C values in Figure 9 are calculated with the most conservative combination of D_S and M_S as $D_S = 6.4$ kpc and $M_S = 0.9M_\odot$ mentioned in subsection A.1 and fixed θ_* of $\theta_* = 0.70\mu$as (thus they are indicated as $M_{\mathrm{C,small}}$ because they are smaller than them calculated with the most likely combination, $D_S = 8.0$ kpc and $M_S = 1.0M_\odot$), while the values in Table 4 include the errors of those parameters. With respect to the χ^2 values of the best fit model parameters, there are few differences between the Xallarap$^K_{bsf}$ and the Xallarap^K models. This is because we set the parameters to calculate $P_{\xi,\mathrm{low}}$ more conservatively than the simple estimate above and it results in $\chi^2_{\mathrm{peri}} \simeq 0$ for the best fit values of the Xallarap^K models.

We can understand how χ^2_{peri} affects the results from Figure 9. The panels showing $M_{\mathrm{C,small}} - \chi^2_{\mathrm{orb}}$ and $M_{\mathrm{C,small}} - \chi^2_{\mathrm{peri}}$ in the figure show that χ^2_{peri} can have a value not 0 with a smaller M_C than the case of χ^2_{orb}. However, contrary to our expectation for χ^2_{peri} to monotonically increase with increasing M_C, a number of links have no penalty, $\chi^2_{\mathrm{peri}} = 0$, even with $M_C > M_{C,\mathrm{max}} = 1.2M_\odot$. This indicates we cannot give a strong constraint on large M_C values with χ^2_{peri}. As shown in $M_{\mathrm{C,small}} - u_{C,0,\mathrm{low}}$ panels, $u_{C,0,\mathrm{low}}$ is determined uniquely with a given M_C. On the other hand, as shown by the $M_{\mathrm{C,small}} - P_{\xi,\mathrm{low}}$ panels, $P_{\xi,\mathrm{low}}$, which determines χ^2_{peri} value dominantly, is not determined uniquely with a given M_C. From the definition, $P_{\xi,\mathrm{low}}$ is dependent on only $\theta_{\mathrm{E}} = \theta_*/\rho$ and u_0 with a given M_C. θ_* is fixed to 0.70 μas and the uncertainty of u_0 ($\sim 4\%$) is much smaller than the uncertainty of ρ ($\sim 30\%$) as shown in Table 2. Therefore it is possible to conclude that the origin of the uncertainty of χ^2_{peri} with a given M_C is the uncertainty of ρ with a given M_C. For example, $\rho - M_{\mathrm{C,small}}$ panels show a width of ρ from $\sim 2 \times 10^{-3}$ to $\sim 8 \times 10^{-3}$, changing by a factor of ~ 4, with $M_C = 1.2M_\odot$. It corresponds to the width of $P_{\xi,\mathrm{low}}$ changing by a factor of ~ 8 with $M_C = 1.2M_\odot$ because $P_{\xi,\mathrm{low}}$ is proportional to $\rho^{-3/2}$. Thus even with a given M_C, a $P_{\xi,\mathrm{low}}$ value can be either larger or smaller than P_ξ. On the other hand, a smaller ρ value makes $P_{\xi,\mathrm{low}}$ larger and thus the constraint of $P_{\xi,\mathrm{low}}$ place a stronger lower limit of ρ than the constraint of $\xi_{\mathrm{E,max}}$. The behaviors of $P_{\xi,\mathrm{low}}$ above resulted that in Xallarap$^K_{bsf}$ models, comparing to Xallarap^K models, we can place a slightly larger lower limit of ρ, give a slightly stronger constraint to an upper limit of M_C and a lower limit of H_C as shown in Table 4. However it still exceeds the brightness limit of H_{excess} and thus we cannot determine the fainter limit of H_L with this constraint.

Our discussions above neglect the case that a companion to the source is a stellar remnant. A black-hole or neutron star is rare relative to a main-sequence star and they are formed with a supernova, an extremely explosive event, so they are extremely rare especially in the case of the companion to a main-sequence star. On the other hand, we cannot reject a white dwarf companion case. However, our constraints work on links with $M_C \gtrsim 0.8M_\odot$ as shown in Figure 9 and white dwarfs with mass of larger than $0.8M_\odot$ are relatively rare (Kepler et al. 2007). Therefore we conclude that our discussion is not likely to be affected by this neglect.

A.3. Comparison with Parallax model

Xallarap$^K_{bsf}$ models have χ^2 differences from the Parallax models by $\Delta\chi^2 > 25$ for 3 more dof. Poindexter et al. (2005) analyzed 22 events where a parallax model improves their light curve fittings compared to the standard model. According to their analysis, there are 3 events that prefer a xallarap model to a parallax model by $\Delta\chi^2 > 25$ in all events they analyzed. They regard it as a strong indication that the light curves of the 3 events have been distorted by xallarap. If a xallarap model explains a parallax signal, the parameters of the xallarap model should mimic the Earth's orbital parameters, namely, the period is $P_\xi \simeq P_\oplus = 1$ yr and the direction is $(R.A._\xi, Dec._\xi) \simeq (R.A., Dec.)_\oplus = (272^\circ, -29.7^\circ)$, the coordinate of this event from the Earth.

To verify our xallarap model, we first plot χ^2 values of the best-fit xallarap model at a fixed P_ξ value within $100 \leq P_\xi(\text{days}) \leq 1500$ in Figure 10. They are shown as $\Delta\chi^2$ values compared to the Parallax close+ model. For this verification, we should compare the Xallarap$^K_{bsf}$ model with a non-constrained xallarap model which has Earth-like parameters. It is because the source system must be a physical one if the xallarap signal is real, but it can have unphysical parameters if the xallarap model mimics a parallax signal. The χ^2 difference between the Xallarap$^K_{bsf}$ model (blue solid line around $P_\xi = 530$ days) and a xallarap model with no constraints around $P_\xi = 365$ days (black solid line around $P_\xi = 365$ days, hereafter Xallarap$_{P_\xi \simeq P_\oplus}$ model) does not exceed $\Delta\chi^2 \simeq 4$. On the other hand, the Xallarap$_{P_\xi \simeq P_\oplus}$ model has a larger χ^2 difference from the Parallax model of $\Delta\chi^2 \simeq 23$. It indicates that the $(R.A._\xi, Dec._\xi)$ of the Xallarap$_{P_\xi \simeq P_\oplus}$ model is inconsistent with the reflection of the direction to the source from Earth's orbital plane. We show the MCMC chain distribution of $(R.A._\xi, Dec._\xi)$ values for the Xallarap$_{P_\xi \simeq P_\oplus}$ model in Figure 11. The black cross indicates the $(R.A., Dec.)_\oplus = (272^\circ, -29.7^\circ)$. There are no link distributed regions in the center of the parameter space we investigated and we find that the $(R.A., Dec.)_\oplus$ is located in the region. From the above, the Earth-like parameters are disfavored from the

aspect of the $(R.A._{\xi}, Dec._{\xi})$ values.

We find that the xallarap models we found are different from the one that mimics a parallax signal. Next, we investigate where the signal comes from in the light curve. Figure 12 shows the same one as Figure 3, but shows the difference between the Xallarap$^{K}_{bsf}$ close+ model and the Parallax close+ model. The χ^2 difference comes from the data in 2013 which is slightly magnified. However, the preference to the parallax model comes almost exclusively from MOA data and the preference from OGLE data is only $\Delta\chi^2 \sim 2$. The MOA data is more easily affected by systematics especially in a low-magnification part because the average seeing on the MOA site is worse than that on the OGLE site. Considering this, it is difficult to claim that the preference of the Xallarap$^{K}_{bsf}$ models over the Parallax models is significant, nor can we claim the Parallax models are more plausible. Thus we dealt with both parallax and xallarap in the main part of the paper.

A.4. Discussion about xallarap analysis

We conducted our fitting for a xallarap model with two observational constraints to obtain a more feasible model and to reduce the brighter limit of the flux of the companion to the source star. As the result, our constraints cannot reduce the brighter limit enough to extract the lens flux from the excess flux by our Keck observations because of the uncertainties of D_S, M_S, $M_{C,\max}$ and θ_* and our conservative treatment for that.

As discussed in subsection A.1, we might constrain the companion brightness sufficiently by including D_S, M_S, θ_* and even isochrone models for the source system as fitting parameters. However it is a very complicated calculation and even with such calculation, the preferred model might not necessarily follow nature because the light curve has some obvious systematics which are not removed. It is found in the fact that without any constraints, the light curve itself prefers unrealistic models which are ruled out by our additional constraints as indicated by black line in Figure 10. More reliably, we can constrain our models more tightly by future follow-up observations with high angular resolution. Furthermore, additional observations are needed to distinguish between parallax models and xallarap models anyway as mentioned in Section 8.

With respect to our new constraint on any undetected binary source signal, we simply used the projected separation as the lower limit of the semi-major axis of the source system like $a_{SC,\mathrm{low}} \equiv D_S \theta_{\mathrm{E}} |u_{C,0,\mathrm{low}} - |u_0||$ when converting $u_{C,0,\mathrm{low}}$, the lower limit of the impact parameter of the companion into the semi-major axis. In principle, we can know the inclination and phase of the source star and the companion at any time in the light curve from xallarap

parameters even including eccentricity. Thus we can calculate the impact parameter $u_{C,0}$ and make the constraint tighter with this information. As for $\chi^2_{\rm peri}$, the additional χ^2, has a substantial uncertainty with a given M_C and takes 0 even with $M_C > M_{C,\rm max}$ because of relatively large uncertainty of ρ ($\sim 30\%$). In other words, the new constraint might affect a massive M_C more efficiently with the event that shows a clear finite source effect.

B. Probability of the contamination fraction f

To estimate a probability of the contamination fraction f, we consider the following three possible sources of contamination: unrelated ambient stars, a companion to the source star and a companion to the lens star (Batista et al. 2014; Fukui et al. 2015).

First, we estimate the probability of contamination owing to unrelated ambient stars. We measured the number density of bright stars with $I < 16$, which is not likely to be affected by blending, in the event field using OGLE-III catalog (Szymański et al. 2011) We then estimated the number density for fainter stars with $I > 16$ by assuming that the luminosity function in the field is same as that in Baade's Window HST observation (Holtzman et al. 1998). Here the differences of extinction and distance between Baade's Window and the event field are adjusted by matching the location of red clump giants in the CMD for both fields (Bennett et al. 2008). Next we convert the excess flux to I-band from $H-$band with $D_S = 8$kpc as $I_{\rm excess} = 18.1$ assuming a mass-luminosity relation (Schmidt-Kaler 1982; Bessell & Brett 1988). We calculate that with $H_{\rm excess} = 17.0$, slightly brighter than Equation (4), conservatively. Counting the number of stars with $I > I_{\rm excess}$, we estimate the number density of stars with brightnesses corresponding to $0 < f < 1$ as 1.82 arcsec^{-2}. Similarly, the number density of stars corresponding to $0.5 < f < 1$ and $0.9 < f < 1$ are estimated as 0.18 arcsec^{-2}, 0.02 arcsec^{-2}, respectively. We can resolve an ambient star only if it is separated from the source by FWHM = 90 mas or more. Thus the probability of contamination owing to unrelated ambient stars within 90 mas around the source, P_{amb}, are $P_{amb}(0 < f < 1) = 4.89\%$, $P_{amb}(0.5 < f < 1) = 0.47\%$ and $P_{amb}(0.9 < f < 1) = 0.04\%$.

Second, we estimate the probability of contamination owing to a companion to the source. Because we can detect a companion on the Keck images if the companion is located far enough from the source and the light curve will be affected if the companion is located close enough to the source, an undetectable companion should be located between the two detection limits. We put the distant limit as 90 mas and the close limit of $a_{SC,\rm low} \equiv D_S \theta_{\rm E} |u_{C,0,\rm low} - |u_0||$ as discussed in subsection A.2 where $u_{C,0,\rm low}$ is defined in Equation (A5). To calculate $u_{C,0,\rm low}$, we obtain $M_{I,C}$ by converting $M_{H,C} = H_{\rm excess} -$

$2.5 \log f - 5 \log (D_S/10\mathrm{pc})$ to $M_{I,C}$ using PARSEC isochrones version 1.2S (Bressan et al. 2012; Chen et al. 2014, 2015; Tang et al. 2014) whereas $M_{I,C}$ is obtained from the companion mass M_C calculated from xallarap parameters in Section A.2. Because $a_{SC,\mathrm{low}}$ and θ_E vary with f, we calculate the probability of contamination owing to a companion to the source using following formula (Fukui et al. 2015, cf.),

$$P(f_1 < f < f_2) = F_\mathrm{binary} \times \int_{f_1}^{f_2} F_{a_c}(f) \times F_{q_c}(f) df \tag{B1}$$

where F_binary is the multiplicity of FGK-dwarfs, $F_{a_c}(f)$ is the fraction of binaries with a separation of $a_{SC,\mathrm{low}}(f) < a_c < 90\mathrm{mas} \times D_S$ and $F_{q_c}(f)df$ is the fraction of binaries with a mass ratio between $q_c(f)$ and $q_c(f+df)$. We derive $M_C(f)$ from $M_{H,C}(f)$ using the PARSEC isochrones version 1.2S for the calculation of $q_c(f)$. We use the distribution of parameters for FGK binaries by Raghavan et al. (2010): $F_\mathrm{binary} = 0.46$ as the multiplicity, a log normal distribution with the mean of $\log P_c(\mathrm{days}) = 5.03$ and the standard deviation of $\sigma_{\log P_c} = 2.28$ as the period distribution and Figure 16 in the paper as the mass ratio distribution. We apply the period distribution by converting a_c to a period using Kepler's 3rd law. Then we obtain $P_{SC}(0 < f < 1) = 22.0\%$, $P_{SC}(0.5 < f < 1) = 3.2\%$, $P_{SC}(0.9 < f < 1) = 0.7\%$ for the Parallax close+ model.

Third, we estimate the probability for contamination owing to a companion to the lens star. In this case, we again use Equation (B1) to calculate the probability because the lens mass, the distance to the lens and the companion mass values are dependent on the f value in addition to θ_E. However, the definition of $F_{a_c}(f)$ is different here. To place close limits on a_c, we consider the shear given by a hypothetical lens companion (Batista et al. 2014). Assuming that we can detect the shear effect when the width of the central caustic created by the companion, $w_c \simeq 4q_c/s_c^2$, is larger than the width of that by the planet, w, we can place a detection limit as $w_c < w$, where s_c is the projected separation normalized by θ_E between the host and a hypothetical companion of the lens. This inequality gives us a close limit on a_c. Adopting 90 mas as the distant limit again, $F_{a_c}(f)$ here is defined as the fraction of binaries with a projected separation of $2\sqrt{q_c(f)/w}\theta_\mathrm{E}(f)D_L(f) < a_c < 90\mathrm{mas} \times D_L(f)$ where $w = 4q/(s - s^{-1})^2 \simeq 0.016 \sim 0.02$ for the close models. We apply $w = 0.02$ to the wide model as well as the close model considering that the shear effect by a hypothetical companion is almost equal to that for the close model because the magnification map on the source trajectory for the wide models is almost same as the close models. Note that uncertainties arising from any assumptions here do not affect the results largely because they are too small compared to the range of a_c values we are considering. We calculate $q_c(f)$ for each f value using isochrone models as well as the source companion case. Because a primary of the lens can be either an M dwarf or FGK dwarf depending on the f value, we use the distributions for FGK-dwarf binaries by Raghavan et al. (2010) for $M_\mathrm{prim}(f) > 0.7$ and that

for KM-dwarf binaries by Ward-Duong et al. (2015) for $M_{\rm prim}(f) \leq 0.7$. Ward-Duong et al. (2015) gives $F_{\rm binary} = 0.347$ as the multiplicity, a log normal distribution with the mean of $\log a_c({\rm AU}) = 0.77$ and the standard deviation of $\sigma_{\log a_c} = 1.34$ as the distribution of the projected separation and a mass ratio distribution that is flat for $0.2 < q_c < 1$ and 0 for $q_c < 0.2$. Integrating Equation (B1) with these distributions and the detection limits, we derive $P_{LC}(0 < f < 1) = 13.7\%$, $P_{LC}(0.5 < f < 1) = 7.2\%$ and $P_{LC}(0.9 < f < 1) = 3.9\%$ for the Parallax close+ model.

Finally, by summing the probabilities for the three sources mentioned above, we can calculate the following total probabilities of contamination: $P(0 < f < 1) = 40.6\%$, $P(0.5 < f < 1) = 10.9\%$, $P(0.9 < f < 1) = 4.6\%$ assuming the Parallax close+ model. Therefore, the probabilities of the contamination fraction not exceeding f shown in Table 3 can be calculated as $P(f \leq 0) = 1 - P(0 < f < 1) = 59.4\%$, $P(f \leq 0.5) = 1 - P(0.5 < f < 1) = 89.1\%$ and $P(f \leq 0.9) = 1 - P(0.9 < f < 1) = 95.4\%$ for the Parallax close+ model.

REFERENCES

Abe, F., Airey, C., Barnard, E., et al. 2013, MNRAS, 431, 2975

Alcock, C., Allsman, R. A., Alves, D., et al. 1995, ApJ, 454, L125

Batista, V., Beaulieu, J.-P., Gould, A., et al. 2014, ApJ, 780, 54

Batista, V., Beaulieu, J.-P., Bennett, D. P., et al. 2015, ApJ, 808, 170

Beaugé, C., & Nesvorný, D. 2013, ApJ, 763, 12

Beaulieu, J.-P., et al. 2006, Nature, 439, 437

Beaulieu, J. P., Bennett, D. P., Batista, V., et al. 2016, arXiv:1601.01846

Bennett, D. P. 2010, ApJ, 716, 1408

Bennett, D. P., Anderson, J., Bond, I. A., Udalski, A., & Gould, A. 2006, ApJ, 647, L171

Bennett, D. P., Batista, V., Bond, I. A., et al. 2014, ApJ, 785, 155

Bennett, D. P., Bhattacharya, A., Anderson, J., et al. 2015, ApJ, 808, 169

Bennett, D. P., Bond, I. A., Udalski, A., et al. 2008, ApJ, 684, 663

Bennett, D. P., & Rhie, S. H. 1996, ApJ, 472, 660

Bennett, D. P., Rhie, S. H., Nikolaev, S., et al. 2010, ApJ, 713, 837

Bennett, D. P., Rhie, S. H., Udalski, A., et al. 2016, ApJ, submitted.

Bensby, T., Yee, J. C., Feltzing, S., et al. 2013, A&A, 549, A147

Bertin, E., & Arnouts, S. 1996, A&AS, 117, 393

Bertin, E., Mellier, Y., Radovich, M., et al. 2002, Astronomical Data Analysis Software and Systems XI, 281, 228

Bessell, M. S., & Brett, J. M. 1988, PASP, 100, 1134

Bond, I. A., Abe, F., Dodd, R. J., et al. 2001, MNRAS, 327, 868

Bonfils, X., Delfosse, X., Udry, S., et al. 2013, A&A, 549, A109

Borucki, W. J., Koch, D., Basri, G., et al. 2010, Science, 327, 977

Boyajian, T. S., van Belle, G., & von Braun, K. 2014, AJ, 147, 47

Bressan, A., Marigo, P., Girardi, L., et al. 2012, MNRAS, 427, 127

Butler, R. P., Wright, J. T., Marcy, G. W., et al. 2006, ApJ, 646, 505

Calchi Novati, S., Gould, A., Udalski, A., et al. 2015, ApJ, 804, 20

Cardelli, J. A., Clayton, G. C., & Mathis, J. S. 1989, ApJ, 345, 245

Carpenter, J. M. 2001, AJ, 121, 2851

Cassan, A., Kubas, D., Beaulieu, J.-P., et al. 2012, Nature, 481, 167

Chen, Y., Girardi, L., Bressan, A., et al. 2014, MNRAS, 444, 2525

Chen, Y., Bressan, A., Girardi, L., et al. 2015, MNRAS, 452, 1068

Claret, A. 2000, A&A, 363, 1081

Dong, S., Gould, A., Udalski, A., et al. 2009, ApJ, 695, 970

Fukui, A., Gould, A., Sumi, T., et al. 2015, ApJ, 809, 74

Gaidos, E., Mann, A. W., Lépine, S., et al. 2014, MNRAS, 443, 2561

Gaudi, B. S., Beaulieu, J. P., Bennett, D. P., et al. 2009, astro2010: The Astronomy and Astrophysics Decadal Survey, 2010,

Gaudi, B. S., Bennett, D. P., Udalski, A., et al. 2008, Science, 319, 927

Gaudi, B. S. 2012, ARA&A, 50, 411

González Hernández, J. I., & Bonifacio, P. 2009, A&A, 497, 497

Gonzalez, O. A., Zoccali, M., Vasquez, S., et al. 2015, arXiv:1508.02576

Gorbikov, E., Brosch, N., & Afonso, C. 2010, Ap&SS, 326, 203

Gould, A. 1992, ApJ, 392, 442

Gould, A. 2000, ApJ, 542, 785

Gould, A., et al. 2006, ApJ, 644, L37

Gould, A., Dong, S., Gaudi, B. S., et al. 2010, ApJ, 720, 1073

Gould, A., & Loeb, A. 1992, ApJ, 396, 104

Gould, A., & Yee, J. C. 2014, ApJ, 784, 64

Han, C., & Gould, A. 2003, ApJ, 592, 172

Han, C., Udalski, A., Choi, J.-Y., et al. 2013, ApJ, 762, L28

Henderson, C. B., Penny, M., Street, R. A., et al. 2015, arXiv:1512.09142

Holtzman, J. A., Watson, A. M., Baum, W. A., et al. 1998, AJ, 115, 1946

Ida, S., & Lin, D. N. C. 2004, ApJ, 604, 388

Ida, S., Lin, D. N. C., & Nagasawa, M. 2013, ApJ, 775, 42

Kennedy, G. M., & Kenyon, S. J. 2008, ApJ, 673, 502

Kepler, S. O., Kleinman, S. J., Nitta, A., et al. 2007, MNRAS, 375, 1315

Kim, S.-L., Lee, C.-U., Park, B.-G., et al. 2016, JKAS, 49, 37

Koshimoto, N., Udalski, A., Sumi, T., et al. 2014, ApJ, 788, 128

Mao, S., & Paczynski, B. 1991, ApJ, 374, L37

Matsakos, T., & Konigl, A. 2016, arXiv:1603.00414

Minniti, D., Lucas, P. W., Emerson, J. P., et al. 2010, New A, 15, 433

Miyake, N., Sumi, T., Dong, S., et al. 2011, ApJ, 728, 120

Muraki, Y., Han, C., Bennett, D. P., et al. 2011, ApJ, 741, 22

Nataf, D. M., Gould, A., Fouqué, P., et al. 2013, ApJ, 769, 88

Penny, M. T., Kerins, E., Rattenbury, N., et al. 2013, MNRAS, 434, 2

Penny, M. T., Henderson, C. B., & Clanton, C. 2016, arXiv:1601.02807

Poindexter, S., Afonso, C., Bennett, D. P., et al. 2005, ApJ, 633, 914

Poleski, R., Skowron, J., Udalski, A., et al. 2014, ApJ, 795, 42

Raghavan, D., McAlister, H. A., Henry, T. J., et al. 2010, ApJS, 190, 1

Sako, T., Sekiguchi, T., Sasaki, M., et al. 2008, Experimental Astronomy, 22, 51

Schmidt-Kaler, Th. 1982, in Landolt-Bornstein: Numerical Data and Functional Relationships in Science and Technology, Vol 2b, ed. K. Schaifers & H. H. Voigt (Berlin: Springer)

Shvartzvald, Y., Maoz, D., Udalski, A., et al. 2016, MNRAS, 457, 4089

Skowron, J., Shin, I.-G., Udalski, A., et al. 2015, ApJ, 804, 33

Skowron, J., Udalski, A., Kozłowski, S., et al. 2016, Acta Astron., 66, 1

Skowron, J., Udalski, A., Poleski, R., et al. 2016, ApJ, 820, 4

Spergel, D., Gehrels, N., Baltay, C., et al. 2015, arXiv:1503.03757

Sumi, T., Abe, F., Bond, I. A., et al. 2003, ApJ, 591, 204

Sumi, T., Bennett, D. P., Bond, I. A., et al. 2010 ApJ, 710, 1641

Sumi, T., Kamiya, K., Bennett, D. P., et al. 2011 ApJ, 473, 349

Sumi, T., Udalski, A., Bennett, D. P., et al. 2016, ApJ, accepted

Suzuki, D., Bennett, D. P., Sumi, T., et al., 2016, ApJ, submitted.

Szabó, G. M., & Kiss, L. L. 2011, ApJ, 727, L44

Szymański, M. K., Udalski, A., Soszyński, I., et al. 2011, Acta Astron., 61, 83

Tang, J., Bressan, A., Rosenfield, P., et al. 2014, MNRAS, 445, 4287

Tsapras, Y., Choi, J.-Y., Street, R. A., et al. 2013, arXiv:1310.2428

Udalski, A. 2003, Acta Astron., 53, 291

Udalski, A., Szymański, M. K., & Szymański, G. 2015, Acta Astron., 65, 1

Udalski, A., Yee, J. C., Gould, A., et al. 2015, ApJ, 799, 237

Verde, L., Peiris, H. V., Spergel, D. N., et al. 2003, ApJS, 148, 195

Ward-Duong, K., Patience, J., De Rosa, R. J., et al. 2015, MNRAS, 449, 2618

Yee, J. C., Shvartzvald, Y., Gal-Yam, A., et al. 2012, ApJ, 755, 102

Yee, J. C. 2015, ApJ, 814, L11

Yee, J. C., Udalski, A., Calchi Novati, S., et al. 2015, ApJ, 802, 76

Yoo, J., DePoy, D. L., Gal-Yam, A., et al. 2004, ApJ, 603, 139

Zhu, W., Udalski, A., Gould, A., et al. 2015, ApJ, 805, 8

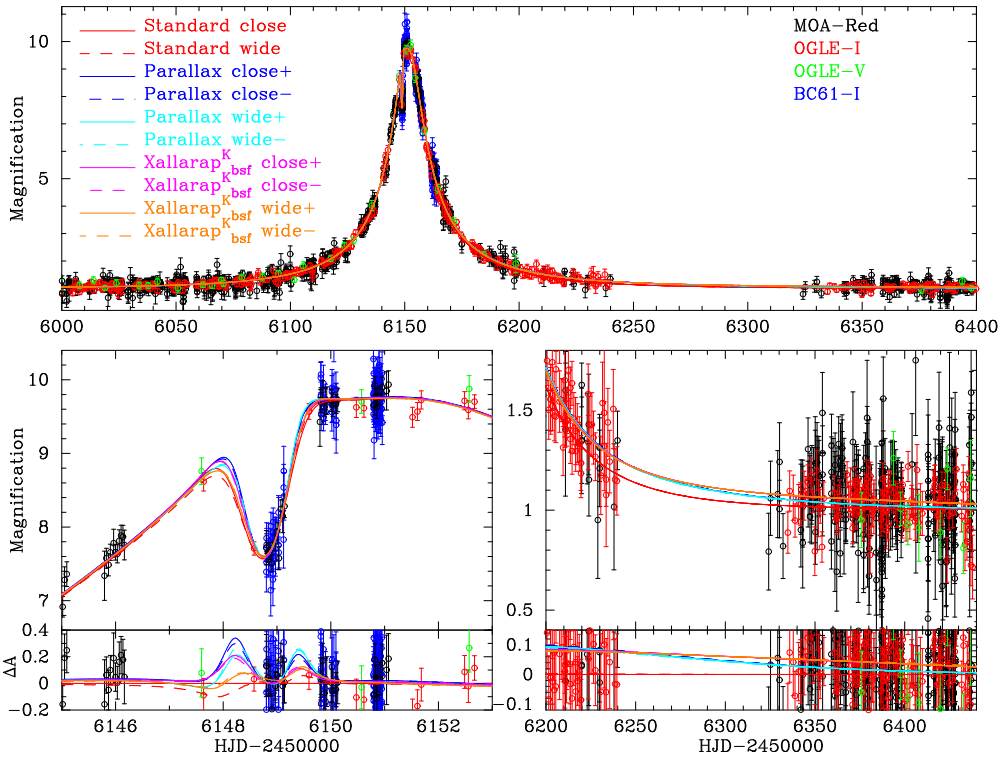

Fig. 1.— The light curve of OGLE-2012-BLG-0950 with the best-fitting models indicated in the top left. The top panel shows the whole event, the bottom left and the bottom right panels highlight the planetary anomaly and the light curve from the end of 2012 to the start of 2013, respectively. The residuals from the Standard close model are shown in the bottom insets of the bottom panels.

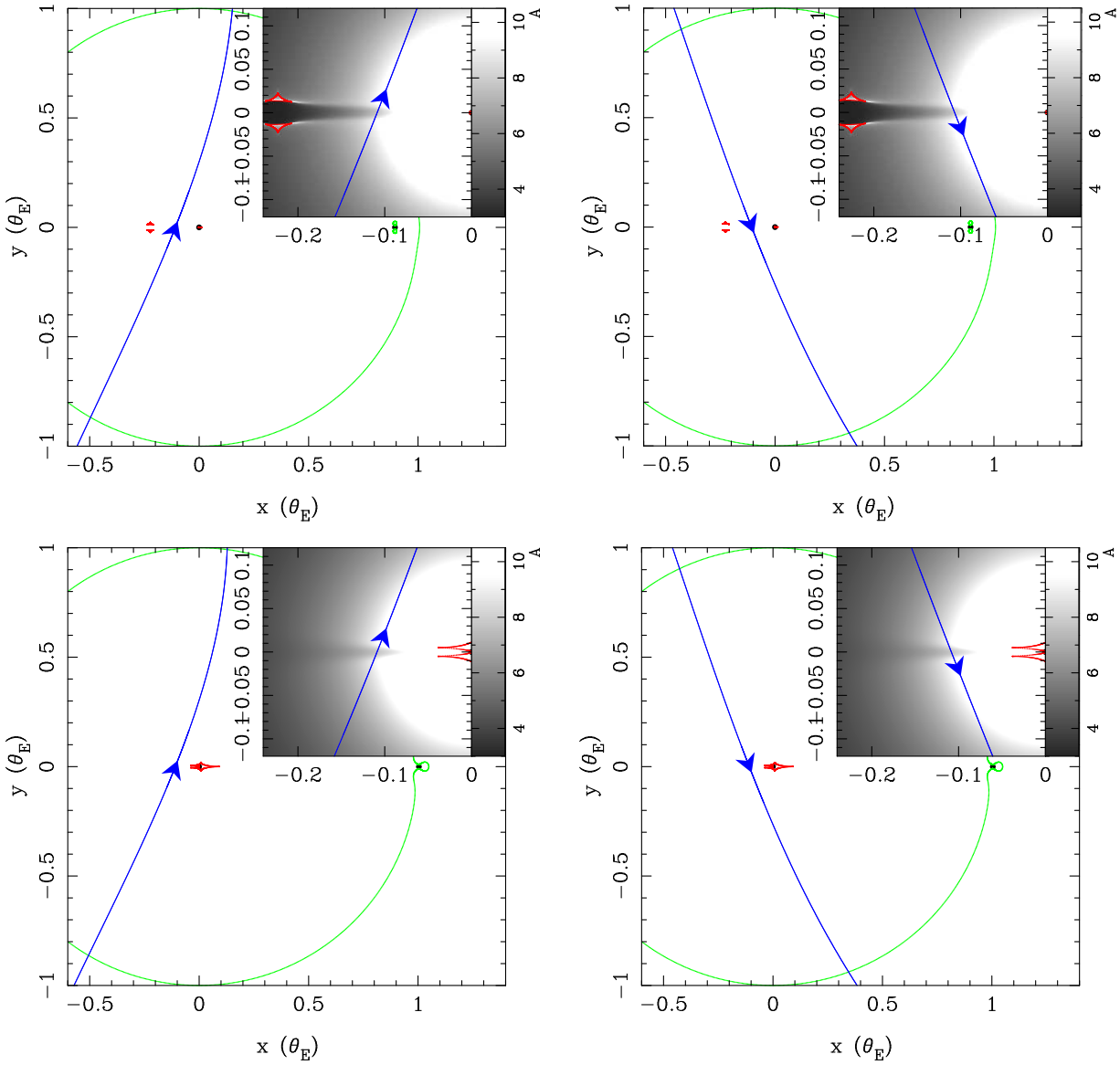

Fig. 2.— Caustics for the Parallax models. The blue arrowed lines indicate the source trajectories. The top left, top right, bottom left and bottom right shows the Parallax close+, close−, wide+ and wide− models, respectively. A magnification map around the anomaly part is shown in the inset of each panel.

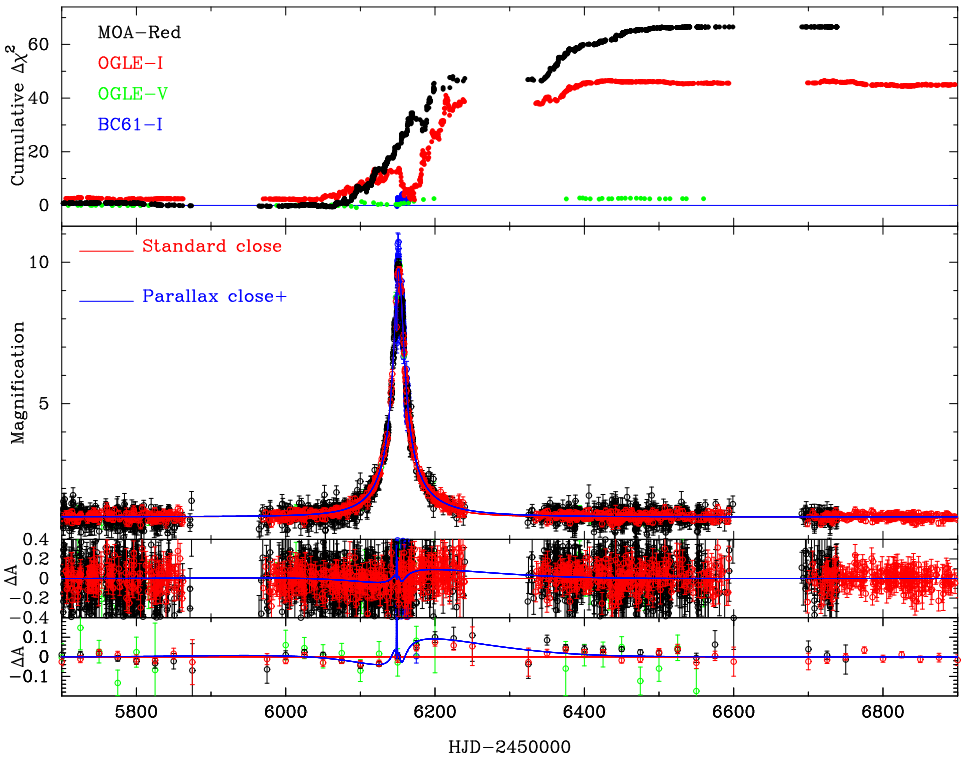

Fig. 3.— Cumulative distribution of $\Delta\chi^2$ between the Standard close model and the Parallax close+ model. Top inset shows the distribution and a positive $\Delta\chi^2$ value indicates smaller χ^2 value of the Parallax close+ than that of the Standard close model. The second and third insets from the top shows the light curve and the residuals from the standard model, respectively. The bottom inset shows the residuals binned by 25 days for clarity.

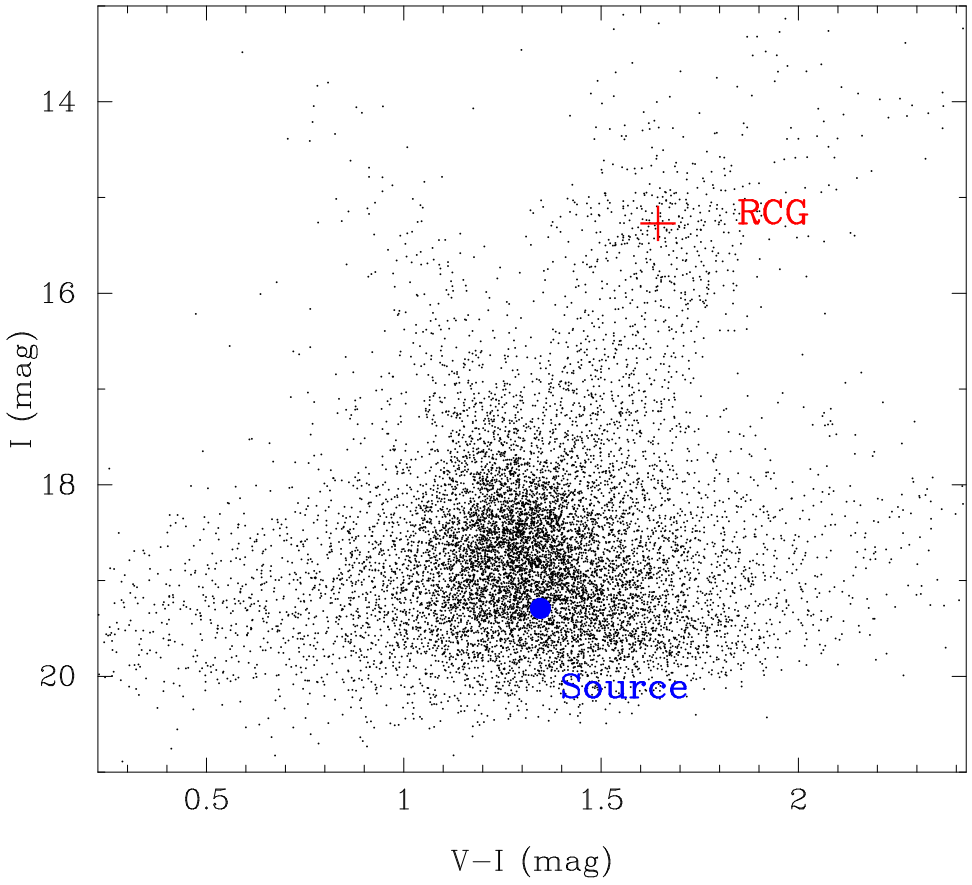

Fig. 4.— The OGLE-IV instrumental color-magnitude diagram of stars within $2' \times 2'$ around the source star. The source star and the mean of red clump giants are shown as the blue filled circle and the red cross, respectively.

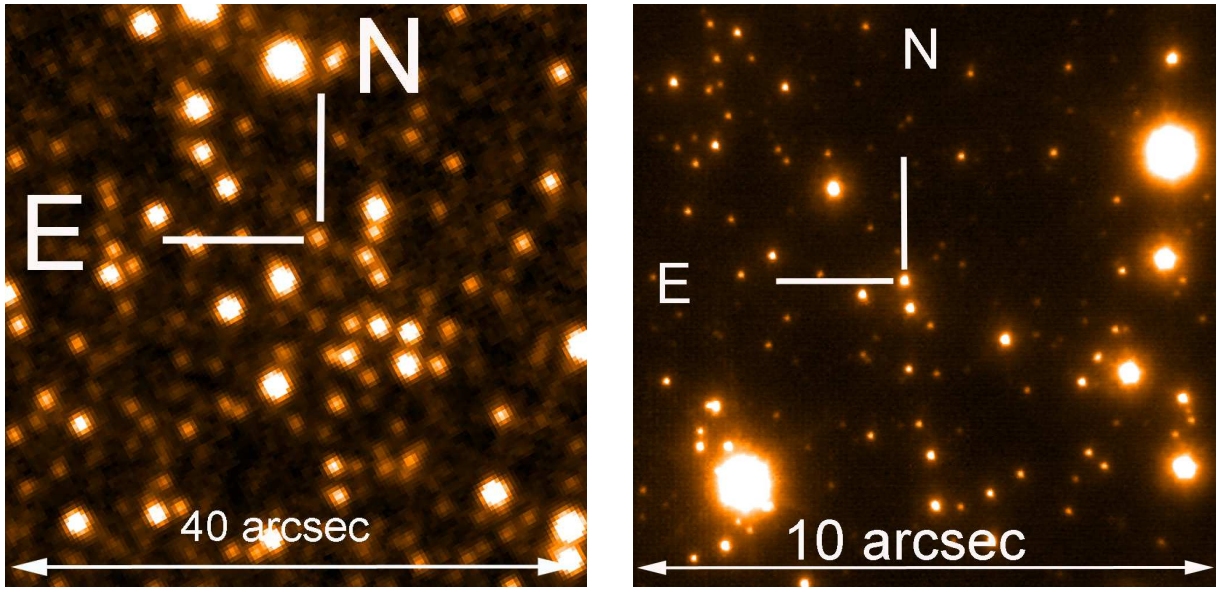

Fig. 5.— Images of the event field observed by VVV (left) and by Keck II (right). The indicated star is the target.

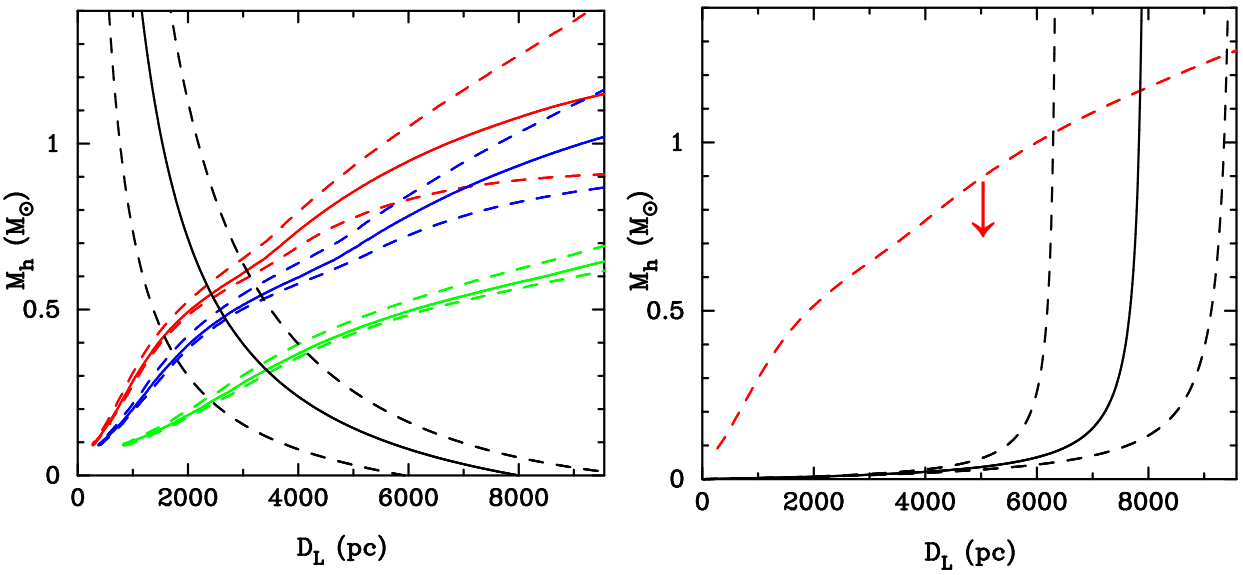

Fig. 6.— Mass-distance relations for the Parallax close+ model (left) and the Xallarap$^{K}_{bsf}$ close+ model (right). The relations from $M_{H,L}$ are shown in red, blue and green for a contamination fraction of $f = 0$, 0.5 and 0.9, respectively. The dashed lines indicate 1 σ error including the uncertainty of the distance to the source, the lens age and the lens metallicity in addition to the uncertainty of our measuring. Black lines are the mass-distance relation come from $\pi_{\rm E}$ (the left) and $\theta_{\rm E}$ (the right). The red arrow in the right panel means that the red dashed line in the panel is just an upper limit.

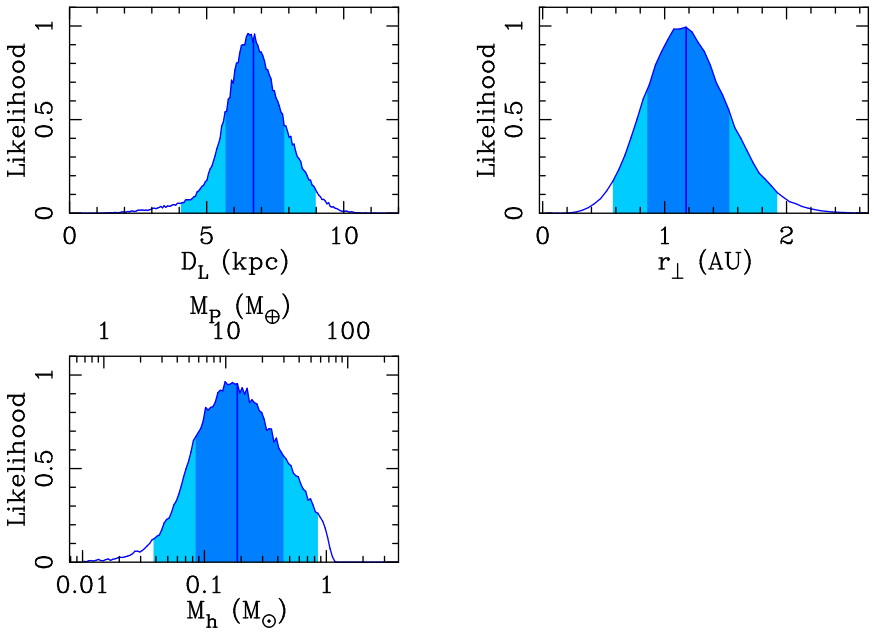

Fig. 7.— Posterior probability distribution of our Bayesian analysis constrained by the observables of the Xallarap$^{K}_{bsf}$ models for the distance to the lens D_L, the mass of the lens system and the secondary $M_{\rm h}$ and $M_{\rm p}$, and the projected separation $r_\perp$. The vertical solid lines indicate the median values. The dark and light shaded regions indicate the 1σ and 2σ limits.

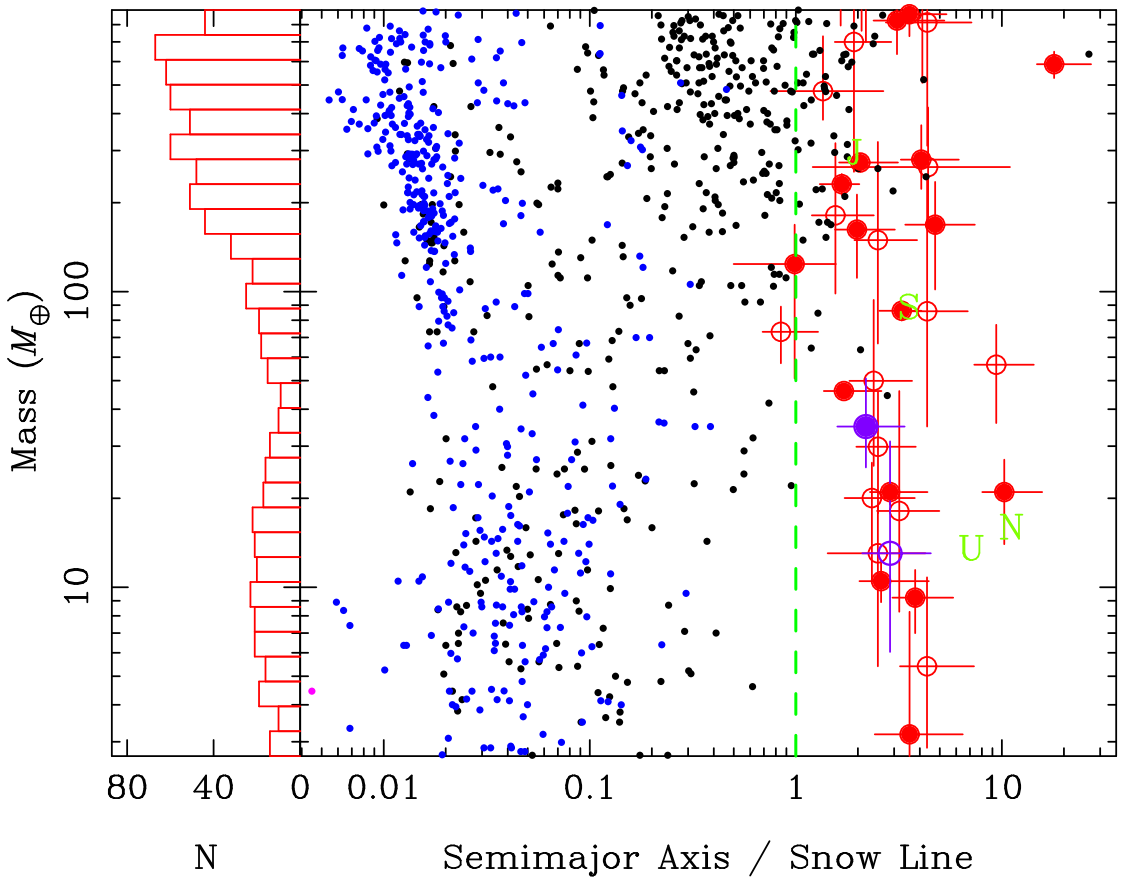

Fig. 8.— Mass versus semi-major axis normalized by the snow-line of discovered exoplanets so far. Here the snow line is estimated by the host star mass as $\sim 2.7M/M_\odot$ (Kennedy & Kenyon 2008). The black and blue dots and red circles indicate planets found by the radial velocity, transit and microlensing, respectively. The results of this work are indicated as the purple circles. In microlensing planets, filled circles indicates that their masses are measured and open circles indicate that their masses are estimated by a Bayesian analysis. A green letter indicates a solar system planets.

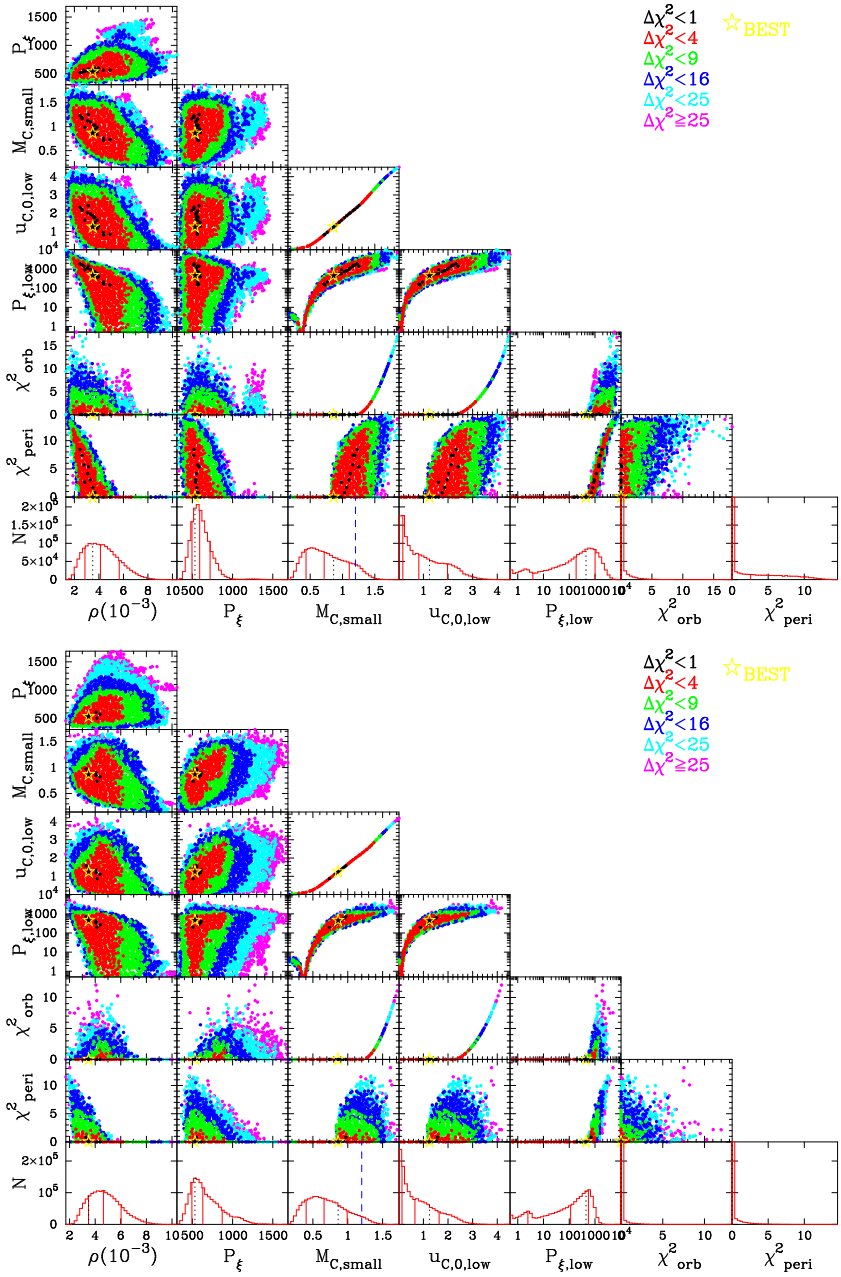

Fig. 9.— MCMC chain distributions of the parameters used to constrain the Xallarap^K close+ model (top panel) and the Xallarap$^K_{bsf}$ close+ model (bottom panel). The color of a dot indicates the χ^2 value. The yellow pentagram in each panel indicates the best-fit value. A histogram in each bottom panel has three red vertical solid lines indicating the 16, 50 and 84 percentiles from the left respectively and one black vertical dotted line indicating the best-fit value. The blue vertical dashed line in the $M_{\rm C,small}$ histogram is the massive limit using our constraints, $M_{C,\rm max} = 1.2 M_\odot$, where $M_{\rm C,small}$ is the companion mass calculated with $D_S = 6.4$ kpc, $M_S = 0.9 M_\odot$ and $\theta_* = 0.70 \mu$as. Note that the uncertainty of the companion mass becomes more larger by including their uncertainties as shown in Table 4.

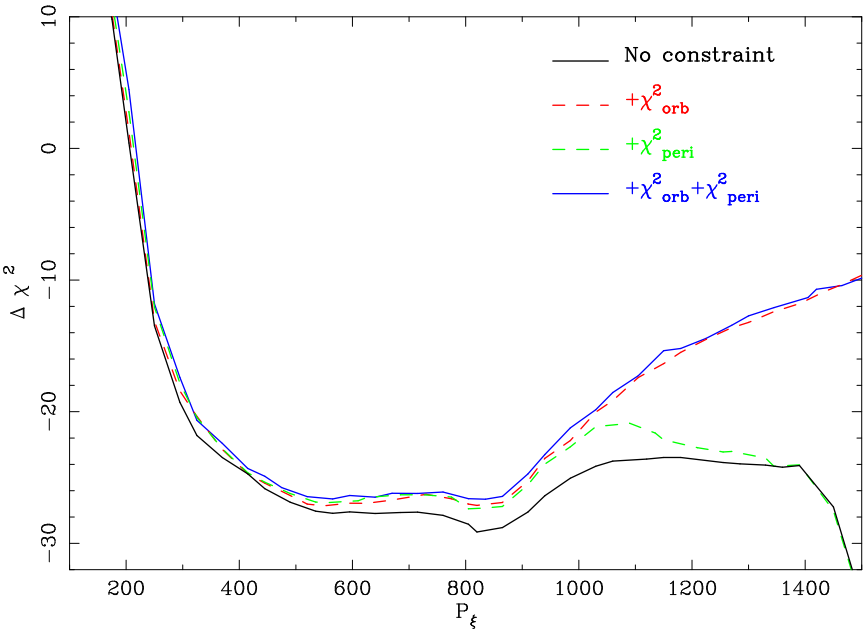

Fig. 10.— $\Delta\chi^2$ between a xallarap model and the Parallax close+ model as a function of orbital period. The black solid, red dashed, green dashed, blue solid lines indicate xallarap models with no constraint, the $\chi^2_{\rm orb}$ constraint (Xallarap^K model), the $\chi^2_{\rm peri}$ constraint and both constraints (Xallarap$^K_{bsf}$ model), respectively, see text.

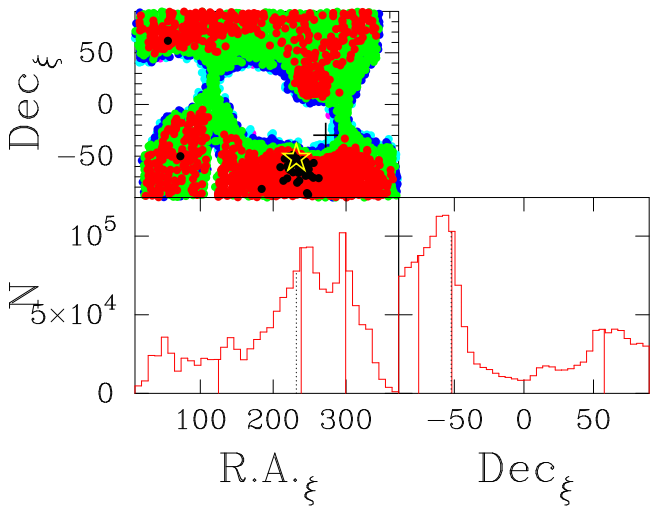

Fig. 11.— MCMC chain distribution of $R.A._\xi$ and $Dec._\xi$ for the Xallarap$_{P_\xi \simeq P_\oplus}$ model. The colors and lines indicated are as described in the caption for Figure 9. The black cross indicates the event $(R.A., Dec.)$ direction from the Earth.

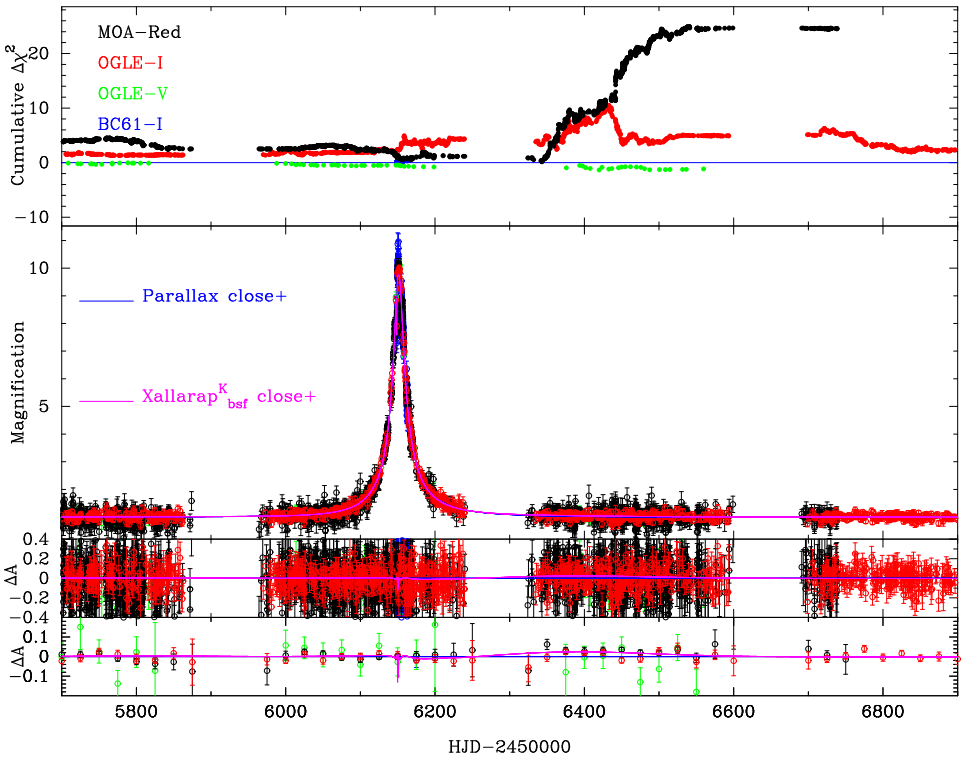

Fig. 12.— As for Figure 3, but showing the difference between the Parallax close+ model and the Xallarap$^K_{bsf}$ close+ model. A positive $\Delta\chi^2$ value indicates a smaller χ^2 of the Xallarap$^K_{bsf}$ close+ model.

Table 1: The data and the parameters for our modeling.

Dataset	Number of data	k	$e_{\min}$	u_λ
OGLE I	1275	1.365	0	0.5470
OGLE V	81	1.576	0	0.7086
MOA-Red	6324	0.981	0	0.5895
B&C I	382	1.017	0.00611	0.5470

Table 2: Model parameters.

Model	t_0 (HJD')	$t_{\rm E}$ (days)	u_0	q (10^{-4})	s	α (rad)	ρ (10^{-3})	$\pi_{E,N}/\xi_{E,N}$	$\pi_{E,E}/\xi_{E,E}$	$\pi_{\rm E}/\xi_{\rm E}$	P_ξ (10^2 days)	I_S (mag)	χ^2	dof
Standard close	6151.58	66.4	0.104	2.3	0.890	5.098	4.3	-	-	-	-	19.26	8168.8	8047
σ	0.03	1.5	0.003	$^{+0.6}_{-0.3}$	0.008	$^{+0.009}_{-0.003}$	< 7.0	-	-	-	-	0.03	-	-
Standard wide	6151.59	66.7	0.104	2.3	1.007	5.100	3.4	-	-	-	-	19.26	8168.1	8047
σ	0.03	1.6	0.003	$^{+0.6}_{-0.2}$	0.008	$^{+0.008}_{-0.004}$	< 6.5	-	-	-	-	0.03	-	-
Parallax close+	6151.47	68.4	0.101	1.9	0.895	5.081	0.0	0.14	-0.19	0.24	-	19.29	8053.2	8045
σ	0.03	1.5	0.003	$^{+0.5}_{-0.1}$	$^{+0.004}_{-0.007}$	0.006	< 3.2	$^{+0.11}_{-0.06}$	0.02	$^{+0.09}_{-0.04}$	-	0.03	-	-
Parallax close−	6151.48	68.5	-0.100	1.9	0.893	1.195	0.0	0.08	-0.17	0.19	-	19.30	8055.8	8045
σ	0.03	1.6	0.003	$^{+0.5}_{-0.2}$	0.006	$^{+0.004}_{-0.007}$	< 3.0	$^{+0.12}_{-0.07}$	0.02	$^{+0.08}_{-0.02}$	-	0.03	-	-
Parallax wide+	6151.49	68.7	0.101	1.9	1.004	5.083	0.0	0.17	-0.20	0.26	-	19.29	8054.7	8045
σ	0.03	1.4	0.003	$^{+0.6}_{-0.1}$	$^{+0.008}_{-0.004}$	0.006	< 3.0	0.08	0.02	0.06	-	0.03	-	-
Parallax wide−	6151.48	67.8	-0.101	1.9	1.004	1.195	0.0	0.09	-0.17	0.19	-	19.29	8057.3	8045
σ	0.02	1.4	0.003	$^{+0.6}_{-0.1}$	$^{+0.009}_{-0.003}$	$^{+0.003}_{-0.009}$	< 3.1	$^{+0.10}_{-0.08}$	0.02	$^{+0.07}_{-0.03}$	-	0.03	-	-
Xallarap^K close+	6151.50	67.2	0.103	2.0	0.894	5.085	3.5	0.0	-0.6	0.6	5.3	19.27	8026.5	8042
σ	$^{+0.04}_{-0.02}$	$^{+2.8}_{-1.1}$	$^{+0.002}_{-0.005}$	$^{+0.5}_{-0.2}$	0.006	$^{+0.012}_{-0.002}$	$^{+2.2}_{-0.6}$	$^{+0.1}_{-0.6}$	$^{+1.0}_{-0.1}$	$^{+0.3}_{-0.2}$	$^{+1.9}_{-0.4}$	$^{+0.06}_{-0.02}$	-	-
Xallarap^K close−	6151.50	66.8	-0.103	2.0	0.895	1.197	3.8	0.1	-0.6	0.6	5.3	19.26	8026.4	8042
σ	$^{+0.04}_{-0.01}$	$^{+3.6}_{-0.7}$	$^{+0.006}_{-0.001}$	$^{+0.5}_{-0.2}$	0.006	$^{+0.003}_{-0.010}$	$^{+2.0}_{-0.8}$	$^{+0.1}_{-0.6}$	$^{+1.0}_{-0.2}$	$^{+0.4}_{-0.2}$	$^{+2.4}_{-0.5}$	$^{+0.07}_{-0.02}$	-	-
Xallarap^K wide+	6151.50	66.7	0.104	2.1	1.005	5.088	2.9	-0.5	-0.3	0.6	5.2	19.26	8027.5	8042
σ	$^{+0.04}_{-0.01}$	$^{+3.6}_{-0.9}$	$^{+0.002}_{-0.006}$	$^{+0.5}_{-0.3}$	$^{+0.007}_{-0.006}$	$^{+0.009}_{-0.005}$	$^{+2.6}_{-0.1}$	$^{+0.6}_{-0.1}$	$^{+0.1}_{-0.6}$	$^{+0.5}_{-0.2}$	$^{+2.7}_{-0.4}$	$^{+0.07}_{-0.02}$	-	-
Xallarap^K wide−	6151.50	66.4	-0.104	2.3	1.006	1.194	3.6	0.0	-0.6	0.6	5.3	19.26	8027.9	8042
σ	$^{+0.04}_{-0.01}$	$^{+4.0}_{-0.3}$	$^{+0.007}_{-0.001}$	$^{+0.3}_{-0.4}$	$^{+0.006}_{-0.007}$	$^{+0.006}_{-0.009}$	$^{+2.0}_{-0.7}$	$^{+0.1}_{-0.6}$	$^{+1.1}_{-0.2}$	$^{+0.5}_{-0.2}$	$^{+2.5}_{-0.5}$	$^{+0.08}_{-0.01}$	-	-
Xallarap$^K_{\rm bsf}$ close+	6151.50	67.2	0.103	2.0	0.894	5.085	3.5	0.0	-0.6	0.6	5.3	19.27	8026.5	8042
σ	$^{+0.04}_{-0.01}$	$^{+3.8}_{-0.9}$	$^{+0.001}_{-0.007}$	$^{+0.5}_{-0.2}$	$^{+0.008}_{-0.005}$	$^{+0.011}_{-0.002}$	$^{+2.5}_{-0.0}$	$^{+0.2}_{-0.7}$	$^{+1.0}_{-0.4}$	$^{+0.6}_{-0.2}$	$^{+3.4}_{-0.4}$	$^{+0.08}_{-0.01}$	-	-
Xallarap$^K_{\rm bsf}$ close−	6151.51	67.1	-0.103	2.0	0.894	1.194	3.5	0.0	-0.5	0.5	5.3	19.27	8026.9	8042
σ	$^{+0.03}_{-0.02}$	$^{+3.6}_{-0.7}$	$^{+0.005}_{-0.002}$	$^{+0.4}_{-0.3}$	$^{+0.008}_{-0.005}$	$^{+0.007}_{-0.006}$	$^{+2.5}_{-0.0}$	$^{+0.2}_{-0.7}$	$^{+0.2}_{-0.5}$	$^{+0.7}_{-0.1}$	$^{+3.0}_{-0.3}$	$^{+0.07}_{-0.02}$	-	-
Xallarap$^K_{\rm bsf}$ wide+	6151.51	66.2	0.104	2.2	1.005	5.089	3.5	-0.5	-0.4	0.6	5.3	19.25	8027.6	8042
σ	$^{+0.03}_{-0.02}$	$^{+3.9}_{-0.4}$	$^{+0.001}_{-0.006}$	0.4	$^{+0.006}_{-0.007}$	$^{+0.008}_{-0.006}$	$^{+2.2}_{-0.0}$	$^{+0.7}_{-0.1}$	$^{+0.7}_{-0.5}$	$^{+0.5}_{-0.2}$	$^{+2.6}_{-0.4}$	$^{+0.08}_{-0.01}$	-	-
Xallarap$^K_{\rm bsf}$ wide−	6151.51	66.6	-0.104	2.2	1.004	1.194	3.5	0.0	-0.6	0.6	5.4	19.26	8027.9	8042
σ	$^{+0.03}_{-0.02}$	$^{+4.3}_{-0.1}$	$^{+0.007}_{-0.001}$	0.4	$^{+0.008}_{-0.006}$	$^{+0.005}_{-0.008}$	$^{+2.3}_{-0.0}$	$^{+0.2}_{-0.7}$	$^{+1.2}_{-0.3}$	$^{+0.6}_{-0.2}$	$^{+3.1}_{-0.5}$	$^{+0.08}_{-0.01}$	-	-

A superscript or subscript of +/− 0.0 indicates that the parameter's best fit value is same as the 84/16 percentile to the given significant digits.

Table 3: Lens properties.

Model	$P(f' \leq f)$ [1] %	θ_* (μas)	$\theta_{\rm E}$ (mas)	μ_{rel} (mas/yr)	$M_{\rm h}$ ($M_\odot$)	$M_{\rm p}$ ($M_\oplus$)	D_L (kpc)	$r_\perp$ (AU)	a (AU)
Parallax									
close+	-	0.69 ± 0.05	> 0.22	> 1.2	> 0.10	> 7	< 5.6	-	-
w/ KECK (f=0)	59.4	-	$1.09^{+0.16}_{-0.10}$	$5.8^{+0.8}_{-0.6}$	$0.57^{+0.06}_{-0.10}$	35^{+10}_{-6}	$2.6^{+0.5}_{-0.7}$	$2.6^{+0.3}_{-0.5}$	$3.1^{+1.5}_{-0.7}$
w/ KECK (f=0.5)	89.1	-	$0.96^{+0.12}_{-0.09}$	$5.1^{+0.6}_{-0.5}$	$0.50^{+0.05}_{-0.09}$	31^{+9}_{-5}	$2.9^{+0.6}_{-0.8}$	$2.4^{+0.2}_{-0.4}$	$3.0^{+1.4}_{-0.5}$
w/ KECK (f=0.9)	95.4	-	$0.64^{+0.06}_{-0.05}$	3.4±0.3	$0.33^{+0.05}_{-0.08}$	21^{+6}_{-4}	$3.6^{+0.6}_{-0.8}$	$2.1^{+0.2}_{-0.3}$	$2.5^{+1.2}_{-0.6}$
close−	-	0.69 ± 0.05	> 0.22	> 1.2	> 0.13	> 9	< 5.8	-	-
w/ KECK (f=0)	58.7	-	$0.99^{+0.18}_{-0.06}$	$5.3^{+1.0}_{-0.3}$	$0.63^{+0.04}_{-0.11}$	41^{+9}_{-7}	$3.2^{+0.4}_{-0.9}$	$2.8^{+0.2}_{-0.5}$	$3.4^{+1.6}_{-0.8}$
w/ KECK (f=0.5)	88.7	-	$0.86^{+0.15}_{-0.06}$	$4.6^{+0.9}_{-0.3}$	$0.55^{+0.03}_{-0.09}$	36^{+8}_{-6}	$3.4^{+0.4}_{-0.9}$	$2.7^{+0.1}_{-0.4}$	$3.3^{+1.5}_{-0.7}$
w/ KECK (f=0.9)	95.1	-	$0.60^{+0.08}_{-0.04}$	$3.2^{+0.4}_{-0.2}$	$0.38^{+0.03}_{-0.08}$	25±5	$4.2^{+0.4}_{-0.9}$	$2.2^{+0.1}_{-0.3}$	$2.7^{+1.3}_{-0.6}$
wide+	-	0.69 ± 0.05	> 0.23	> 1.2	> 0.11	> 8	< 5.5	-	-
w/ KECK (f=0)	60.2	-	$1.14^{+0.11}_{-0.15}$	$6.1^{+0.6}_{-0.8}$	$0.54^{+0.09}_{-0.07}$	34^{+13}_{-4}	$2.4^{+0.8}_{-0.5}$	2.7±0.4	$3.3^{+1.9}_{-0.7}$
w/ KECK (f=0.5)	89.3	-	$0.99^{+0.08}_{-0.13}$	$5.3^{+0.4}_{-0.7}$	$0.47^{+0.08}_{-0.07}$	30^{+11}_{-4}	$2.6^{+0.8}_{-0.5}$	2.6±0.4	$3.2^{+1.8}_{-0.6}$
w/ KECK (f=0.9)	95.6	-	$0.66^{+0.04}_{-0.07}$	$3.5^{+0.2}_{-0.4}$	$0.31^{+0.07}_{-0.05}$	20^{+8}_{-3}	$3.4^{+0.8}_{-0.5}$	2.2±0.3	$2.7^{+1.5}_{-0.5}$
wide−	-	0.69 ± 0.05	> 0.23	> 1.2	> 0.13	> 9	< 5.8	-	-
w/ KECK (f=0)	58.9	-	$0.99^{+0.17}_{-0.06}$	$5.3^{+0.9}_{-0.4}$	$0.63^{+0.05}_{-0.10}$	39^{+13}_{-4}	$3.2^{+0.4}_{-0.9}$	$3.1^{+0.2}_{-0.5}$	$3.8^{+1.9}_{-0.8}$
w/ KECK (f=0.5)	88.8	-	$0.87^{+0.14}_{-0.07}$	$4.7^{+0.8}_{-0.4}$	$0.55^{+0.04}_{-0.09}$	34^{+11}_{-4}	$3.4^{+0.4}_{-0.9}$	$3.0^{+0.2}_{-0.4}$	$3.6^{+1.8}_{-0.8}$
w/ KECK (f=0.9)	95.1	-	$0.60^{+0.07}_{-0.04}$	$3.2^{+0.4}_{-0.2}$	$0.38^{+0.04}_{-0.08}$	24^{+8}_{-3}	$4.2^{+0.4}_{-0.9}$	$2.5^{+0.1}_{-0.3}$	$3.1^{+1.5}_{-0.6}$
Mean	-	0.69 ± 0.05	$0.99^{+0.26}_{-0.19}$	$5.3^{+1.4}_{-1.0}$	$0.56^{+0.12}_{-0.16}$	35^{+17}_{-9}	$3.0^{+0.8}_{-1.1}$	$2.7^{+0.6}_{-0.7}$	$3.4^{+2.4}_{-1.1}$
Xallarap$^K_{bsf}$									
close+	-	$0.71^{+0.04}_{-0.07}$	$0.20^{+0.00}_{-0.09}$	$1.1^{+0.0}_{-0.5}$	-	-	-	-	-
w/ KECK	-	-	-	-	< 1.17	< 78	< 9.4	< 1.7	-
close−	-	$0.70^{+0.05}_{-0.06}$	$0.20^{+0.00}_{-0.09}$	$1.1^{+0.0}_{-0.5}$	-	-	-	-	-
wide+	-	$0.71^{+0.04}_{-0.07}$	$0.20^{+0.00}_{-0.08}$	$1.1^{+0.0}_{-0.5}$	-	-	-	-	-
wide−	-	$0.70^{+0.05}_{-0.06}$	$0.20^{+0.00}_{-0.08}$	$1.1^{+0.0}_{-0.5}$	-	-	-	-	-
w/ Bayesian [2]	-	-	0.19±0.04	1.0±0.2	$0.19^{+0.26}_{-0.10}$	13^{+18}_{-7}	$6.7^{+1.1}_{-1.0}$	$1.2^{+0.4}_{-0.3}$	$1.3^{+0.8}_{-0.4}$

A superscript or subscript of +/− 0.0 indicates that the parameter's best fit value is same as the 84/16 percentile to the given significant digits

[1] Probability of contamination fraction not exceeding f.

[2] According to the posterior probability derived by the prior probability and likelihood from observed value.

Table 4: 1 σ possible value ranges of mass and H magnitude of the source companion and $P_{\xi,\mathrm{low}}$ for xallarap models.

Model	M_C ($M_\odot$)	H_C (mag)	$P_{\xi,\mathrm{low}}$ (10^2 days)
Xallarap^K			
close+	0.57 - 1.71	16.3 - 20.4	0.04 - 10.06
close−	0.56 - 1.71	16.3 - 20.5	0.03 - 9.76
wide+	0.62 - 1.81	16.1 - 20.7	0.09 - 10.82
wide−	0.60 - 1.76	16.2 - 20.2	0.02 - 10.76
Xallarap$^K_{bsf}$			
close+	0.52 - 1.50	16.5 - 20.7	0.02 - 5.53
close−	0.54 - 1.56	16.5 - 20.6	0.03 - 5.73
wide+	0.58 - 1.59	16.4 - 20.3	0.05 - 5.99
wide−	0.58 - 1.60	16.4 - 20.3	0.06 - 6.18

The range of 1 σ error is shown for each parameter.